X-ray Spectroscopy of Accretion Disks and Stellar Winds in X-Ray Binaries

Duane A. Liedahl and Patrick S. Wojdowski

Department of Physics and Advanced Technologies, Lawrence Livermore National Laboratory, P.O. Box 808, Livermore, CA 94550

Mario A. Jimenez-Garate and Masao Sako

Columbia Astrophysics Laboratory and Department of Physics, Columbia University, 538 West 120th Street, New York, NY 10027

Abstract.
From hot, tenuous gas dominated by Compton processes, to warm, photoionized emission-line regions, to cold, optically thick fluorescing matter, accreting gas flows in X-ray binaries span a huge portion of the parameter space accessible to astrophysical plasmas. The coexistence of such diverse states of material within small volumes (10^{33}–10^{36} cm^3) leaves X-ray spectroscopists with a challenging set of problems, since all such matter produces various X-ray spectral signatures when exposed to hard X rays. Emission-line regions in X-ray binaries are characterized by high radiation energy densities, relatively high particle densities, and velocities ~ 1000 km s^{-1}. In this article, we describe some recent efforts to generate detailed X-ray line spectra from models of X-ray binaries, whose aims are to reproduce spectra acquired with the *ASCA*, *Chandra*, and *XMM-Newton* observatories. With emphasis on the global nature of X-ray line emission in these systems, the article includes separate treatments of high-mass and low-mass systems, as well as summaries of continuum spectroscopy and plasma diagnostics.

1. Basic Concepts

1.1. X-Ray Binaries

An X-ray binary (XRB) consists of a compact object—a neutron star or black hole—that is accreting material from another (companion) star. XRBs comprise the brightest class of extrasolar X-ray sources, and have been subjected to nearly four decades of study. In the Galaxy, about 200 XRBs have been catalogued (van Paradijs 1995) and grouped into two major subdivisions: low-mass X-ray binaries (LMXB; with companion mass $M_c \lesssim 1 M_\odot$) and high-mass X-ray binaries (HMXB; $M_c \gtrsim 10 M_\odot$), each with a number of subclassifications in use in the current literature (White 1989).

In the broadest astronomical context, XRBs owe their significance to their status as products of exotic stellar evolution. In a similar vein, XRBs provide some of the best opportunities to observe the extreme endpoints of stellar evo-

lution, in which issues such as dense matter and strong gravity come to the fore. Accretion physics plays a role in all of these subject areas—we learn about neutron stars and black holes by watching matter fall onto (or into) them. With the advent of spaceborne X-ray detectors with high spectral resolving power comes new, highly-detailed information to inform our understanding of mass transfer in XRBs. With respect to *Chandra* and *XMM-Newton*, it is too early to provide a thorough review of the advances made possible by these new missions. We will, therefore, keep the article somewhat general, and concentrate on X-ray spectroscopy and modeling, and leave "what-we-have-learned" reviews for the future. A series of review articles covering most of the major topics associated with XRBs is contained in Lewin, van Paradijs, & van den Heuvel (1995). A number of earlier review articles concerning the specifics of XRBs are in the literature. Among them are Nagase (1989), White (1989), White & Mason (1985), and White, Swank, & Holt (1983).

While the source of accretion material in both HMXBs and LMXBs is a nearby companion star, the physical processes by which the material is transferred to the collapsed star differ. For LMXBs, a gaseous disk mediates the transfer, the disk being fed by Roche lobe overflow; for HMXBs, the UV field of the early-type companion drives a wind through which the accretor moves, sweeping up a small fraction of the wind through gravitational capture. There are exceptions, and it is worth noting that some HMXBs appear to be powered by Roche lobe overflow, so that this classification scheme (LMXB/disk: HMXB/wind) is not strictly adhered to. The best studied XRBs typically have high accretion luminosities (10^{36}–10^{38} erg s^{-1}), owing to the ready availability of matter to accrete (large $\dot{M}$) and to the compactness of the region in which kinetic energy is converted into high-energy radiation ($L_x \propto \dot{M}/R_x$).

In LMXB accretion disks, the nearly circular quasi-Keplerian annuli have projected velocities of $\sim 10^3 \sin i\, (M/M_\odot)^{1/2} R_{10}^{-1/2}$ km s^{-1}, for inclination angle i, where $R_{10} = R/(10^{10}$ cm$)$. In HMXBs, to the extent that we are observing reprocessing in stellar winds, comparable velocities are expected. Large scale velocity fields should broaden the lines, and, in some instances, shift them, as well. With a few exceptions, the ability to measure the effects of velocity fields, made possible by the high resolving power of the $XMM - Newton$ Reflection Grating Spectrometer (RGS) and, especially, the *Chandra* High Energy Transmission Grating (HETG), represents a new dimension in X-ray spectroscopy of XRBs, and promises to provide valuable constraints on source models.

Even with the highest angular resolution available with X-ray telescopes, XRBs cannot be spatially resolved, as they subtend roughly 100 μarcsec at a distance of 1 kpc. The X-ray spectrum measured at Earth is thus a composite of spectra formed over a large volume and, presumably, over a wide range of physical conditions. If we assume that the continuum is born pure at its site of formation, then we can think of the interaction of the continuum radiation with the accreting gas as deforming the continuum. The magnitude of the continuum deformation varies wildly from source to source, and, for a given source, usually varies on observable time scales as well. The spectral imprinting by circumsource material provides, in principle, a set of handles that observers/analysts can use to construct a physically and geometrically consistent model of the source.

1.2.   Emission Processes

Continuum deformation in XRBs is the result of four main types of process: continuum absorption, discrete emission and recombination continuum emission, resonant scattering, and Compton scattering. If local material intervenes with our line of sight to the continuum source, then absorption may alter the shape of the continuum, sometimes producing observable photoelectric edges. The X-ray irradiated gas in the vicinity of the continuum source radiates lines and continua characteristic of the local conditions. This gas can also intercept continuum radiation at energies corresponding to atomic level separations. A photon can be absorbed, and subsequently re-emitted at nearly the same energy, but with a new direction. This can either add to or subtract from the photon flux propagating toward the observer, depending on the location of the reprocessing gas with respect to the observer's line of sight to the continuum source. Finally, in plasmas in which the abundant elements are stripped of their electrons, Compton scattering can regulate the rate of energy exchange between the gas and the radiation field, and can, depending on the Compton depth and the electron temperature, produce substantial modification to the spectrum. The resulting composite spectrum is further modified by its passage through the interstellar medium. Since most XRBs lie near the Galactic plane at distances $\gtrsim 1$ kpc, this is significant, in effect "cutting off" most sources at wavelengths longward of 20–30 Å.

We emphasize emission-line spectroscopy in this article, and, for the most part, restrict the discussion to the 1–35 Å band, since there are no observable atomic features shortward of 1 Å, and most XRBs cannot be observed in the X-ray band at wavelengths longward of 35 Å. The key emission processes are briefly described below.

To generalize each of the reaction types, we denote by *core* an atomic configuration and by *(core) nl* the same configuration modified by the addition of an electron described by the quantum numbers n and l. The symbols e and $h\nu$ are used for free electrons and photons, respectively.

Electron-Ion Impact Excitation

$$(core)\ nl + e \rightarrow (core)\ n'l' + e'$$
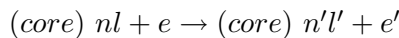
While electron temperatures in X-ray photoionized plasmas are too low (see §1.3) to effectively populate high-lying energy levels by electron impact excitation (EIE), this process is often the dominant one in transferring population between closely-spaced levels. Important instances of EIE are the collisional de-population of the energy level responsible for the so-called forbidden line in He-like ions ($1s^2$-$1s2s\ ^3S_1$), and the populating of low-lying excited states in L-shell and M-shell ions.

Radiative Recombination

$$core + e \rightarrow (core)\ nl + h\nu$$
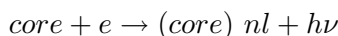
The outgoing photons are distributed into a continuum—the radiative recombination continuum (RRC)—above the recombination edge ($E = \chi$), with a width $\Delta E \approx kT_e$. In an overionized plasma $\Delta E/E \approx kT_e/\chi \ll 1$, which means that

the recombination continuum feature is narrow, and appears "line-like." To date, the only identified RRC features have been associated with recombination to the ground level of H-like and He-like ions, but more often recombination leaves an ion in an excited state.

Dielectronic Recombination In this two-step process, the first step, radiationless capture, excites an electron belonging to the initial-state ion—no photon is emitted.

$$(core) + e \rightarrow (core)' \, nl$$
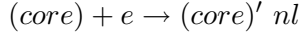
In X-ray photoionized plasmas, the core is excited by way of an intrashell transition, such as $2s \rightarrow 2p$. The energy of the ion following capture lies above the first ionization limit. The ion may, therefore, autoionize. For example,

$$(core)' \, nl \rightarrow core + e',$$
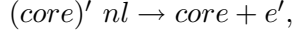
which is, in effect, an elastic scatter when combined with the first step. Alternatively, the ion can emit a photon, leaving the ion with an energy below the first ionization limit (*radiative stabilization*), which completes the dielectronic recombination (DR), for example,

$$(core)' \, nl \rightarrow (core)' \, n'l' + h\nu_o.$$

DR is not an important process for K-shell ions, but can be the dominant recombination mechanism for L-shell ions.

Radiative Cascade

$$(core) \, nl \rightarrow (core) \, n'l' + h\nu_o$$
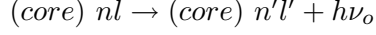
Subsequent to recombination into an excited level, the ion will decay in a series of spontaneous radiative transitions, until it reaches the ground level. At each step the ion may have access to several decay channels. The relative probabilities attached to these various channels partly determine the ionic spectrum. At high densities, however, EIE can interrupt the cascade, possibly resulting in line ratios that differ noticeably from the low-density limit. For ions with L-shell electrons, cascades following both RR and DR must be considered. Since the post-DR stabilized state can have an excited core, cascades that proceed in the presence of a "frozen" excited core are possible, the spectrum of which is distinct from the RR cascade spectrum. Since collisional excitation of high-lying states is exceptionally rare in X-ray photoionized plasmas, radiative cascades following recombination are of paramount importance, which can be contrasted to the case of collisionally-ionized plasmas, where, in the context of line spectroscopy, recombination processes are generally treated as details.

Fluorescence

$$1s^2 \, (nl)^N + h\nu \rightarrow 1s \, (nl)^N + e$$
$$1s \, (nl)^N \rightarrow 1s^2 \, (nl)^{N-1} + h\nu_K$$
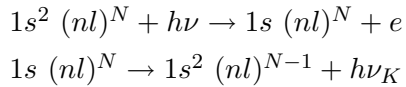
A two-step process. Here the initial state "core" is written as the composite of a closed $n = 1$ shell plus N additional bound electrons. The first step is a K-shell photoionization. In the second step one of the N electrons above the K shell fills the K shell, emitting a characteristic K photon. If the falling electron originates in $n = 2$ (L shell), then the photon is designated Kα. The probability that the second step above occurs, rather than autoionization

$$1s \ (nl)^N \rightarrow 1s^2 \ (nl)^{N-2} + e'$$
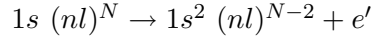
is called the fluorescence yield, which scales as Z^4. Owing in part to the rapid scaling with Z, fluorescence lines from iron are the most commonly observed. In principle, calculating the fluorescence spectrum is a computationally intensive problem. A full calculation of the Kα fluorescent spectrum of a few-times-ionized ion would require a determination of the level population distribution of numerous low-lying energy levels, consistent with the local electron density and radiation field. The fact that many levels can have non-trivial population densities in XRBs not only affects the exact distribution of fluorescent lines but drastically increases the number of radiative and autoionization transitions that need to be calculated. In practice, however, these complications are ignored. In particular, the redistribution of Kα line emission cannot be resolved with current instruments. The effect on fluorescent yields is not known in general (cf., Jacobs et al. 1989).

1.3. The Ionization Parameter

The physical conditions in optically thin X-ray photoionized gas are, for a given ionizing spectrum, conveniently parameterized by the *ionization parameter*. Although there are a number of quantities dubbed "ionization parameter" in the literature, most of what follows is discussed in terms of ξ (Tarter, Tucker, & Salpeter 1969), the use of which is motivated by consideration of the steady-state equations of ionization equilibrium. Let β_i, C_i, and α_{i+1} denote the photoionization rate (s^{-1}) of charge state i, the collisional ionization rate coefficient (cm^3 s^{-1}) of i, and the recombination rate coefficient (cm^3 s^{-1}) of charge state $i + 1$, respectively. The term α_{i+1} accounts for all two-body recombination processes. In steady state the equations of ionization equilibrium can be written

$$\beta_i n_i + n_e C_i(T_e) \ n_i = n_e \alpha_{i+1}(T_e) \ n_{i+1}, \tag{1}$$

where the temperature dependence of the rate coefficients is indicated. Given the photoionization cross-section σ_i and ionization threshold energy χ_i of charge state i, the photoionization rate for a point source of ionizing continuum can be written

$$\beta_i = \frac{L_x}{r^2} \ \int_{\chi_i}^{\infty} dE \ \frac{S_E(E)}{4\pi E} \ \sigma_i(E), \tag{2}$$

where S_E is the spectral shape function, normalized on a suitable energy interval. Denoting the integral in Eq. (2) by Φ_i, Eq. (1) becomes

$$\frac{L_x}{n_e r^2} \ \Phi_i \ n_i + C_i(T_e) \ n_i = \alpha_{i+1}(T_e) \ n_{i+1}. \tag{3}$$

Let $\xi = L_x/n_e r^2$, which is called the *ionization parameter*. Then

$$\frac{n_{i+1}}{n_i} = \frac{C_i(T_e) + \xi\Phi_i}{\alpha_{i+1}(T_e)} \tag{4}$$

Equation (4) shows that an X-ray photoionized plasma with temperature T_e is overionized with respect to collisional ionization equilibrium, owing to the presence of the $\xi\Phi_i$ term. A useful way to think about overionization is that for a given level of ionization the plasma is cool compared to the equilibrium temperature corresponding to collisional ionization equilibrium (the limit $\xi \to 0$). The simultaneous solution of the set of ionization equations (Eq. 4) and the energy equation (*heating = cooling*) gives the $T_e(\xi)$ relation. It is found that C_i can usually be neglected for the photoionized plasmas of interest to X-ray spectroscopists. Such plasmas are thus purely X-ray photoionized.

1.4. X-Ray Photoionization Codes

Thorough treatments of photoionization codes and their applications can be found in Davidson & Netzer (1979), Ferland et al. (1998), and Kallman & Mc-Cray (1982). In short, photoionization codes are used to determine the effect of a radiation field on a gas of specified chemical composition, and the self-consistent effect that passage through the gas has on the radiation field, including the addition of local sources of radiation. This entails, among other things, the determination of the charge state distribution and temperature as functions of ξ. Maxwellian electron distributions are assumed, but LTE is not. LTE is rarely applicable, owing to the insufficiently high electron densities and the highly-diluted non-Planckian radiation fields found in XRBs. Calculations are performed in the spirit of *detailed level accounting*, whereby charge state fractions and level populations are calculated by explicit inclusion of all relevant rates into and out of each energy level. It is found that highly-ionized ions exist over the approximate range 10–10^4 in ξ (c.g.s. units). Below that range recombination lines fall at energies below the X-ray band, but inner-shell fluorescence line emission is still possible. Above that range, ions are fully stripped, but hydrogen-like recombination emission is still possible. Recombination spectra are formed primarily in the approximate temperature range 10^5-10^6 K.

2. Spectral Diagnostics in X-Ray Photoionized Plasmas

One of the themes of this article is the global nature of line formation in XRBs. In other words, even simple models of the geometric and physical distribution of gas in XRBs show that lines form over regions comparable in size to the binary systems themselves, often encompassing a broad range of physical conditions. That the volume integral of the line emissivity determines the observed line ratios and line profiles in a non-trivial way should be kept in mind. Attempting to infer the run of physical conditions in a source by solving the inverse problem using a set of line ratios is problematic when working outside the framework of a particular model of the source. Nevertheless, it is always useful to take advantage of spectral features or line ratios that are, for example, sensitive to temperature or density, in order to provide a starting point for more detailed studies. In

this section, a few of the available discrete diagnostics are discussed. A more detailed treatment of X-ray spectroscopy of photoionized plasmas, with emphasis on atomic kinetics, is given in Liedahl (1999). A more general presentation of X-ray spectroscopy, including discussions of the relevant atomic rates, can be found in Mewe (1999).

2.1. Signatures of Dominance by X-Ray Photoionization

Although X-ray line emission in XRBs is likely to originate in photoionized gas, one still seeks explicit confirmation through examination of spectra. After all, it is conceivable that XRBs contain regions of, for example, shock-heated gas. The indicator of photoionization dominance is recombination dominance in the emission line spectra of high charge states. Having discerned that the emission mechanism is consistent with pure recombination, one can then appeal to photoionization codes in order to assign a rough value of ξ, from the $f_i(\xi)$ relationship, and T_e, from the $T_e(\xi)$ relationship, both derived for the appropriate ionizing continuum. Fortunately, there are a few easily recognized spectral signatures of recombination dominance, described below.

(1) *Presence of Narrow RRC.* As discussed in §1.3, an X-ray photoionized plasma is overionized, i.e., the electron temperature is much less than the ionization temperature. This condition leaves recombination as the dominant level populating mechanism (see §1.2). X-ray lines produced by radiative cascades following recombination are accompanied by (often) narrow RRC. In the optically thin limit the ratio is a weak function only of temperature. For H-like ions, for example, the ratio $I(1s\text{-}2p)/\text{I(RRC)}$ is approximately 1.3 (Liedahl & Paerels 1996). Since RRC shapes are determined by T_e, RRC provide a relatively model-independent temperature diagnostic, and can, in principle, be used to check the theoretical $T_e(\xi)$ relationship.

(2) *Large* G *ratio in He-like ions.* The He-like G ratio is defined as the intensity ratio $(x + y + z)/w$, where x and y are the intercombination lines $1s^2 \ ^1S_0$–$1s2p \ ^3P_{2,1}$, z is the forbidden line $1s^2 \ ^1S_0$–$1s2s \ ^3S_1$, and w is the resonance line $1s^2 \ ^1S_0$–$1s2p \ ^1P_1$ (Gabriel & Jordan 1969). In collisional ionization equilibrium w is the brightest He-like line, while in photoionization equilibrium in the low-density limit, z is the brightest (Pradhan 1985; Liedahl 1999). Thus a "by-eye" examination of the ratio z/w may be sufficient to discern photoionization/recombination dominance. At higher densities, however (see next section), the blend $x + y$ can be brighter than z, so, to generalize, the sum $x + y + z$ is used in the definition of G. In short, a large G ($\approx$ 3-4) implies that recombination dominates, while $G \approx 1$ implies collisional ionization (Bautista & Kallman 2000; Porquet & Dubau 2000). With velocity fields of a few $\times$ 1000 km s^{-1}, line broadening can cause x and y to blend with w, so that G cannot be trivially specified, and other combinations of the lines may need to be used (Paerels et al. 2000).

(3) *Relatively weak or apparent absence of iron L-shell emission in presence of K-shell emission from lighter elements.* Decades of solar X-ray observations have familiarized spectroscopists with the fact that bright iron L-shell emission dominates the line spectrum of cosmic-abundance plasmas with temperatures

in the 10^6-10^7 K range (Phillips et al. 1982). It was shown by Kallman et al. (1996), however, that under conditions of overionization, iron L-shell emission is overwhelmed by $1s - np$ and RRC emission from K-shell ions of, for example, oxygen, neon, and magnesium. There are several reasons for this. Perhaps the simplest way to look at it is to think of iron L-shell ions as having unusually large collisional rate coefficients, which help to drive the impressive line fluxes observed in collisionally ionized plasmas, but do not come into play at all in photoionized plasmas. These calculations have been borne out by the *ASCA* observation of the HMXB Vela X-1 during eclipse (Nagase et al. 1994), which shows a spectrum dominated by H-like and He-like ions. In fact, Sako et al. (1999) achieved satisfactory fits to the data using an otherwise detailed spectral model for which iron L-shell spectra were entirely absent. Recombination spectra also affect iron L-shell ratios (Liedahl et al. 1990) but it appears that use of these ratios may have to wait for instruments of higher sensitivity.

2.2.   The R Ratio in He-like Ions

We have already remarked on the use of He-like ions to discriminate between collisional ionization and photoionization. They are also well known density diagnostics (Gabriel & Jordan 1969). The useful ratio is denoted by R, and is defined as $R = z/(x+y)$, where x, y, and z were defined in the previous section. The z line is a slow magnetic dipole transition, so that as n_e increases, collisional depopulation of the $1s2s\ ^3S_1$ level begins to compete with radiative decay. The density at which the rates of these two depopulation mechanisms are equal is called the critical density n_{crit}. The dominant sinks for the outgoing population flux are the three $1s2p\ ^3P$ levels, two of which can decay to ground, producing the x and y lines. Thus the ratio R decreases with increasing n_e.

The density dependence of R is well approximated by $R = R_o\left[1+(n_e/n_{crit})\right]^{-1}$, where R_o is the zero-density limit of R. The variation of R is greatest for the two orders of magnitude in n_e centered on n_{crit}. Below this range, one would observe $R \approx R_o$, and assign an upper limit to n_e. Above this range, $R \approx 0$, and a lower limit can be assigned.

The ground state transitions of He-like ions of C, N, O, Ne, Mg, Si, S, Ar, Ca, and Fe fall into the X-ray band. Both R_o and n_{crit} vary with Z (Pradhan 1982), and obtaining their theoretical values requires detailed solutions of the rate equations (Bautista & Kallman 2000; Porquet & Dubau 2000). In particular, n_{crit} increases with Z, ranging from $\sim 10^9$ cm^{-3} for C V to $\sim 10^{17}$ cm^{-3} for Fe XXV. To the extent that the various He-like spectra are present in a given set of data, density information is available over a broad region of n_e–ξ parameter space.

The prevalence of He-like ions in highly-ionized plasmas, the relative simplicity of calculating He-like spectra, and their sensitivity to plasma conditions has made them the pre-eminent diagnostics in X-ray spectroscopy. However, a complication that was noted early on in the study of He-like spectra is now being revisited, one which may compromise the use of the R diagnostic in some systems, notably XRBs. The collisional transitions that are crucial to the density sensitivity of He-like ions, $1s2s\ ^3S_1 \rightarrow 1s2p\ ^3P_{0,1,2}$ are all electric dipole transitions, and can be driven equally well by photons. The wavelengths corresponding to the energy separation of the $1s2s\ ^3S_1$ and $1s2p\ ^3P_1$ levels, to take

an example, are 1634 Å, 1273 Å, and 868 Å, for O, Ne, and Si, respectively. A bright UV source in the vicinity of the X-ray emission-line regions can thus have the effect of mimicking the signature of high electron density.

The possible influence of UV radiation on R was pointed out by Gabriel & Jordan (1969) for solar applications, where it was found that only C V should be affected by photospheric UV emission, and by Blumenthal, Drake, & Tucker (1972), who emphasized that, for example, the presence of a moderately hot white dwarf could drive the R ratio to low values. This has obvious implications for HMXBs, in which O and B stars reside, and LMXBs, in which an accretion disk emits copious UV radiation. It was argued by Kahn et al. (2001) that the low values of R observed in the isolated O supergiant ζ Pup are consequences of UV driving, rather than high densities, consistent with expectations that stellar winds are too tenuous for the collisional depopulation of the $1s2s\ ^3S_1$ level to matter. However, if our expectations are that densities *should* be high enough for the collisional mechanism to work, and a UV source is also present, a genuine "degeneracy" occurs. This may be the case in LMXBs (Liedahl et al. 1992) and some classes of cataclysmic variable. What is needed is another X-ray density diagnostic, one that is not susceptible to UV driving, and one for which the critical density lies in an interesting part of parameter space. One such candidate is the Ne-like Fe XVII 17.10/17.05 ratio ($n_{\mathrm{crit}} \sim 10^{13}$ cm^{-3}), which appears to be immune to the influence of few-eV Planckian radiation fields (Mauche, Liedahl, & Fournier, in preparation).

3.   Photoionizing Continua in XRBs

The X-ray spectra of XRBs are almost completely dominated by continuum radiation, most of which is thought to be produced through conversion of the gravitational potential energy of the accreted material into radiation. Apart from the nearly ubiquitous iron K complex, detections of discrete line emission have, prior to *ASCA*, been difficult to obtain, owing to the limited sensitivity of X-ray spectrometers, and partly to the small intrinsic equivalent widths of the emission lines. In the case of HMXBs, where most of the soft X-ray line emission originates from an extended stellar wind, the mass-loss rates of the companion stars are typically $\dot{M} \sim 10^{-6}\ M_\odot$ yr^{-1}, which implies photoelectric optical depths $\tau_{\mathrm{pe}} \ll 1$ for most of the relevant charge states. In LMXBs, where the lines are produced near the surface of an accretion disk, the solid angle subtended by the disk at the continuum source is $\Delta\Omega/4\pi \sim 0.1$–0.2. Thus in either case only a small fraction of the source X-ray luminosity leaves the system in the form of discrete X-ray emission. Still, recent observations of HMXBs and LMXBs with high-sensitivity, high-resolution spectrometers show discrete features that can be used to constrain models of the structure of the accretion flow around compact objects (Brandt & Schulz 2000; Cottam et al. 2001).

Despite the large variety of XRBs, all of them have one common property— they emit strong continuum radiation over several decades in energy. The X-ray luminosities of persistent XRBs are intrinsically variable, and range anywhere from (typically) $L_x \sim 10^{36}$ erg s^{-1} during the low state to as high as the Eddington luminosity of a few $\times 10^{38}$ erg s^{-1}. In black hole X-ray novae, the range in X-ray luminosities is more dynamic, with quiescent luminosities as low as

$L_x \sim 10^{30}$ erg s^{-1} (Garcia et al. 2000). A large fraction of XRBs, however, are persistent X-ray sources.

The intrinsic continuum shape and the location of the source determine the ionization and thermal structure of the surrounding photoionized medium, and, as such, are important for interpreting the associated emission/absorption line features imprinted on the continuum spectrum. On the other hand, these structures do not depend on the physical mechanism responsible for the production of the primary continuum radiation. Therefore, the line spectrum cannot be used to infer *how* the continuum is generated.

From an observational point-of-view, the spectral shape of the continuum radiation from XRBs is well-understood, in the sense that they can be reproduced by relatively simple mathematical prescriptions. In neutron star HMXBs, for example, the X-ray continuum can usually be described by a single power law with photon indices in the range $\Gamma = 1.2$–2.0, with an exponential cut-off at energies above $E_c \gtrsim 10$ keV, and e-folding energies of $E_f \sim 10$–30 keV (Nagase 1989). A possible physical interpretation of this spectrum is unsaturated Comptonization of soft seed photons as they travel through a hot, fully-ionized medium. When the observed spectrum covers a wide enough range in energy, measurements of the power-law slope and the cut-off energy provide simultaneous estimates of the electron temperature and optical depth of the Comptonizing medium, as demonstrated by Eardley, Lightman, & Shapiro (1975) and Sunyaev & Titarchuk (1980) using the hard X-ray continuum spectrum observed in the HMXB Cygnus X-1. Most HMXBs contain pulsars, which makes the radiation field anisotropic as well as time-dependent. The illuminated circumsource medium, therefore, responds to either the instantaneous flux or the time-averaged flux, depending on the gas density and the pulse-period. Electron cyclotron absorption and/or emission features are also seen in the hard X-ray spectra of many HMXBs, and can be used to estimate the magnetic field strength of the neutron star (Trümper et al. 1978; Wheaton et al. 1979)

In LMXBs, single-component continuum models usually do not provide adequate fits to the data (see White, Nagase, & Parmar 1995 and references therein). The spectrum, instead, typically consists of a cut-off power law similar to those seen in HMXBs, but with an additional blackbody component with temperatures of $kT_{bb} \sim 1$ keV, the latter presumably originating from the boundary layer between the accretion disk and the neutron star surface. In many cases, the blackbody component is observed to be more variable than the Comptonized component, implying that it is not the source of seed photons for Comptonization (White, Peacock, & Taylor 1985). There is also evidence for the blackbody component to be point-like, whereas the harder Comptonized spectrum originates from a more extended region (Church et al. 1998), providing further support for the picture described above. Mitsuda et al. (1984) demonstrated that the use of multi-colored blackbody models (as a replacement for the Comptonized component) provide constraints on the inner radius of the emitting region. However, White, Stella, & Parmar (1988) argue that multi-colored blackbody emission models do not provide adequate descriptions of the spectra of most LMXBs, and are, moreover, physically implausible, since electron scattering should modify the shapes of the intrinsic spectra (Shakura & Sunyaev 1973).

The fact that the continuum shape can be parametrized by simple phenomenological models makes it difficult to infer the physical mechanisms responsible for continuum radiation production. Various physical models can produce continuum spectra of similar shape, and the data usually cannot be used to distinguish between different models, especially when the data cover a relatively narrow band pass (e.g., Vacca et al. 1987). For example, a $kT \sim 10$ keV bremsstrahlung spectrum cannot be distinguished from Comptonized emission in a mildly Compton thick medium. If each of the components are absorbed through different (or time varying) column densities, the continuum parameters derived under the assumption of a single absorbing column may provide purely empirical results that have little to do with reality. Sometimes, the degeneracy can be broken by studying the temporal behavior of the continuum during the various spectral states, as well as quasi-periodic oscillations (QPOs) in different energy bands.

Many theoretical models have been developed in an attempt to unify the global spectrum and the temporal behavior of XRBs. For disk accretion onto weakly-magnetized neutron stars Lamb (1989), Lamb & Miller (1995), and Psaltis, Lamb, & Miller (1995) proposed a physically self-consistent model, which describes the spectra and the QPOs during the various states. In this model, the neutron star magnetosphere produces soft X-ray seed photons through electron cyclotron emission, which are Comptonized within the magnetosphere itself, as well as in a hot corona that forms around the magnetosphere. More recently, the development of various branches of self-consistent accretion flow solutions such as advection-dominated accretion flows (ADAF; Ichimaru 1977; Narayan & Yi 1995) that successfully describe the spectral behavior of black hole XRBs (Tanaka & Lewin 1995; Tanaka & Shibazaki 1996), advection-dominated inflow/outflow systems (ADIOS; Blandford & Begelman 1999), and convection-dominated accretion flows (CDAF; Quataert & Gruzinov 2000) have provided us with deeper insights about the global energetics of accretion flows around compact objects.

4. X-Ray Spectroscopy of Stellar Winds in HMXBs

Using the first X-ray satellite *Uhuru*, Schreier et al. (1972) showed that periodic changes in the X-ray pulse frequency of Cen X-3 could be used to establish the binarity of the system. This observation, along with the finding that the optical candidate of Cyg X-1 was a spectroscopic binary (Bolton 1971; Webster & Murdin 1972), was a key to confirming suggestions that many of the bright variable X-ray sources known at the time were indeed close binaries (Shklovsky 1967 proposed that Sco X-1 is a neutron star binary). The *Uhuru* observations of Cen X-3 showed that during X-ray eclipses the X-ray flux level did not go to zero but that there was a residual flux, indicating the presence of extended matter, or, in any case, another source of X rays in the system. Cen X-3 was soon identified in the optical with an O-type star (Krzemiński 1974). Early type stars had already been known to have strong winds with mass loss rates $\dot{M} \sim 10^{-6}$ $M_\odot$ yr^{-1} and velocities $v \sim 1000$ km s^{-1} (Morton 1967). Thus it was natural to attribute the residual eclipse flux in Cen X-3 to scattering or other reprocessing by a stellar wind. Similar explanations were given for the residual

flux observed in other eclipsing X-ray binary pulsars identified with early-type stars, such as Vela X-1, 4U 1538-522, SMC X-1, and LMC X-4.

The hard X-ray continuum spectrum of the residual eclipse radiation was generally observed to have the same form as the uneclipsed flux in the hard X-ray band. Therefore, electron scattering, which is independent of photon energy for small Compton y parameters and photon energies such that $h\nu \ll m_e c^2$, was implicated as the reprocessing mechanism (e.g., Becker et al. 1978). The residual flux observed in eclipse is usually a few percent of the flux outside of eclipse, implying scattering optical depths τ_e of a few percent. To get an estimate of the corresponding electron density, we let the companion star set the linear scale ($R_\star \sim 10 R_\odot$), and estimate n_e from $\tau_e = n_e R_\star \sigma_T$, where σ_T is the Thomson cross section. This gives a density $\sim 10^{10}$ cm^{-3} in HMXB winds, which is consistent with the densities in the winds of isolated massive stars.

The wind provides a natural source of accretion fuel to power the X-ray source. For the wind density derived above, the theory of Bondi & Hoyle (1944) predicts an accretion rate sufficient to power a neutron star luminosity of approximately $10^{36} v_{1000}^{-3}$ erg s^{-1}, where v_{1000} is the wind velocity in multiples of 1000 km s^{-1}. Therefore, while it is possible that, in some HMXBs, the compact object is powered by accretion directly from a wind of the type found in isolated massive stars, those that lie at the high end of the luminosity range are not easily accommodated. Either the wind must be much different than in an isolated massive star wind (for example, the wind velocity is much lower), or the compact object must be fueled in some other manner, such as Roche lobe overflow.

For a luminosity of 10^{36}–10^{38} erg s^{-1}, the density and length scale described above imply ξ values in the range 10^2–10^4. For such large ionization parameters, astrophysically abundant elements are typically ionized up to the K shell (e.g., Kallman & McCray 1982). If we note additionally that the electron temperatures implied for such gas are 10^5–10^7 K, then we can estimate line luminosities. For Si XIV Lyα, for example, the recombination line luminosity is

$$L_{\text{line}} = n_e n_H A_{\text{Si}} \ VF\alpha_{\text{eff}} \ E_{\text{line}}, \tag{5}$$

where E_{line} is the line photon energy, V is the volume of the emission region, F is the ionization fraction of fully stripped silicon, A_{Si} is the silicon abundance relative to hydrogen, and α_{eff} is the effective rate coefficient for recombinations that result in emission of a Si XIV Lyα photon. If we use the density and length scale from above, take the solar abundance of silicon, assume that silicon is fully stripped ($F = 1$), and $\alpha_{\text{eff}} = 4.2 \times 10^{-12}$ cm^3 s^{-1} (for a temperature of 100 eV; Osterbrock 1989) then we find a value of approximately $L_{\text{line}} \approx 10^{32}$ erg s^{-1}. The continuum spectra of X-ray pulsars are typically flat (photon index of -1) up to approximately 10 keV, above which they are cut off. So, the specific monochromatic luminosity of the continuum is approximately $(L_X/10\,\text{keV})$. In eclipse, since the apparent luminosity is reduced to a few percent of that outside of eclipse, the monochromatic luminosity becomes 10^{33} erg s^{-1} keV^{-1}. This gives equivalent widths ~ 100 eV, which are easily observable with *ASCA*. With the benefit of hindsight, we see that lines from highly-ionized gas might have been expected. It was somewhat surprising to many of us, however, when Vela X-1 was observed over an eclipse, and several emission lines from H-like and He-like ions were observed (Nagase et al. 1994).

Before the launch of *ASCA* in 1993, X-ray spectroscopy provided information on the winds of HMXBs mostly through studies of scattering and absorption of the continuum. The properties of the scattered continuum are almost entirely independent of the physical state and chemical composition of the scattering gas. This is useful, in that studies of the X-ray scattered continuum "find" all of the gas, but problematic, in that the electron scattered continuum conveys no information on the physical state of the gas. Absorption tends to probe regions of low ionization, and provides a valuable complement to studies of emission lines (e.g., Haberl, White, & Kallman 1989) from highly ionized regions. The iron K emission line complex provided some constraints on the state of gas in the pre-*ASCA* era but with proportional counters, the 6.4, 6.7, and 6.9 keV lines of neutral or near-neutral, helium-like, and hydrogen-like iron, respectively were often blended. The absence of detailed information regarding the state of the highly-ionized gas has compromised our ability to describe the wind physics because the mechanism by which the wind is accelerated is likely to depend on the local temperature and ionization state.

4.1. Ionization of Stellar Winds by an X-ray Source

In massive, isolated stars, winds are driven as UV photons from the star transfer their outward momentum to the wind via absorption line transitions. Castor, Abbott, & Klein (1975) showed that line transitions provide the opacity to power winds in isolated, massive stars, and that the winds obey the velocity law

$$v(R) = v_\infty \left(1 - \frac{R_\star}{R}\right)^\beta,$$ (6)

for a given distance R from the center of the wind donor, where $R_\star$ is the stellar radius, and where $\beta = 0.5$, assuming a UV point source. By accounting for the finite size of the companion star, Pauldrach, Puls, & Kudritzki (1986) showed that values of β in the range 0.7–1.0 are better representations of the wind kinematics.

Given a velocity profile, the wind density can be calculated by applying the equation of mass continuity, assuming spherical symmetry:

$$n(R) = \frac{\dot{M}}{4\pi\mu m_p v(R) R^2},$$ (7)

where μ is the gas mass per hydrogen atom. We can estimate the density from this equation and compare it to our earlier estimate based upon inferred Compton depths. For $\mu = 1.4$,

$$n = 2 \times 10^{10} \left(\frac{\dot{M}}{10^{-6} \ \mathrm{M_\odot \ yr^{-1}}}\right) \left(\frac{v}{10^8 \ \mathrm{cm \ s^{-1}}}\right)^{-1} \left(\frac{R}{10^{12} \ \mathrm{cm}}\right)^{-2} \ \mathrm{cm^{-3}}, \quad (8)$$

which provides some validation to expectations that a more or less normal stellar wind is responsible for reprocessing the central X-ray continuum.

If a point source of X rays is introduced into this system such that the distance of a gas parcel from the source is denoted by r, then from Eqs. (6) and

(7), the ionization parameter of a smooth wind is

$$\xi = \frac{4\pi\mu m_p L v_\infty}{\dot{M}} \left(\frac{R}{r}\right)^2 \left(1 - \frac{R_\star}{R}\right)^\beta. \tag{9}$$

Contours of constant $\log\xi$ for a representative set of parameters are plotted in Fig. 1. With a strictly spherically symmetric wind, i.e., ignoring the effects of non-inertial forces in the co-rotating frame, stellar rotation, etc., the line of centers is an axis of cylindrical symmetry. Since recombination timescales near the binary are short compared to the orbital period, this structure is virtually fixed in the co-rotating frame, modulo intrinsic time variations in the X-ray continuum flux. This type of configuration was first studied by Hatchett & McCray (1977). Surfaces of constant ξ are surfaces of fixed charge state distribution, as well as constant temperature.

At large r (and, therefore, large R) both the wind density and the ionizing flux fall as $r^{-2} \approx R^{-2}$, and ξ approaches a constant value $\xi_0 = 4\pi\mu m_\mathrm{p} L_\mathrm{x} v_\infty/\dot{M}$, or, numerically

$$\xi_0 \approx 50 \left(\frac{L_x}{10^{36}\ \mathrm{erg\ s^{-1}}}\right) \left(\frac{v_\infty}{10^8\ \mathrm{cm\ s^{-1}}}\right) \left(\frac{\dot{M}}{10^{-6}\ M_\odot\ \mathrm{yr^{-1}}}\right)^{-1}\ \mathrm{erg\ cm\ s^{-1}}. \tag{10}$$

More significantly, ξ_0 is also close to the values of ξ at points on the system midplane ($r = R$; ξ on the midplane is exactly equal to ξ_0 for the limiting case $\beta = 0$). This latter aspect provides a way to estimate a characteristic value of ξ for a particular system, since most of the X-ray emission will originate in the binary system between the companion and the X-ray source.

What Fig. 1 does not show, of course, is the n_e^2 weighting needed to calculate line emissivities $j(n_\mathrm{e}, \xi) = n_\mathrm{e}^2 P(\xi)$, where P is the line power (c.g.s. dimensions erg cm^3 s^{-1}). If the ξ structure for a particular system is such that a given ion can exist in regions near the companion star, then, for lines emitted by this ion, these denser regions of the irradiated stellar wind will have the highest line emissivities. On the other hand, the luminosities of lines formed at somewhat higher ξ, produced away from the stellar surface, benefit from the larger volumes ΔV_line over which they can form ($L_\mathrm{line} \sim j_\mathrm{line}\Delta V_\mathrm{line}$). Moving away from the companion, the competition between the falloff in density and the increase in the volume over which lines form determines the weightings given to each ion in producing the overall recombination line spectrum. The coupling of models for the ionization structure and the wind velocity profile provides the means by which to calculate this distribution in weightings, called the *differential emission measure distribution*, discussed in the next section. It turns out, however, that ξ_0 is a good indicator of the spectrum, in the sense that prominent lines will be produced in regions characterized by values of ξ centered approximately on ξ_0.

The high level of ionization in the wind induced by the X-ray source causes a serious complication in the simple picture presented above. Studies of the effects of X rays on the wind-driving mechanism have shown that the radiative force decreases as wind material becomes increasingly ionized by the X-ray source (MacGregor & Vitello 1982; Stevens & Kallman 1990). As predicted by Hatchett & McCray (1977), this effect can be observed directly through the orbital phase variation of resonance lines of UV P Cygni profiles from ions such as
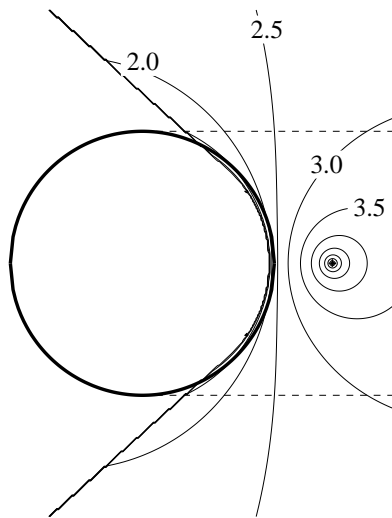
Figure 1.   Contours of $\log \xi$ in an HMXB with a smooth β-law wind (Eq. 9), assuming the following parameters: $L = 10^{37}$ erg s^{-1}; $\dot{M} = 10^{-6}$ $M_{\odot}$ yr^{-1}; $v_{\infty} = 10^8$ cm s^{-1}; $\beta = 0.8$; $R_{\star} = 10$ $R_{\odot}$; and $a = 15$ $R_{\odot}$. The line of centers is an axis of cylindrical symmetry. Dashed lines delineate the part of the stellar wind occulted by the companion star at orbital phase 0.0 (center of X-ray eclipse). Diagonal lines tangent to the companion delineate the shadow cone—the part of the wind shielded from direct radiation from the point X-ray source.

Si IV, C IV, and N V (Dupree et al. 1980; Hammerschlag-Hensberge, Kallman, & Howarth 1984; Vrtilek et al. 1997). Stevens (1991), in one-dimensional numerical simulations, calculated the effect of X-ray photoionization on the wind dynamics in HMXBs, and was unable to find outflowing wind solutions for X-ray luminosities larger than a few times 10^{36} erg s^{-1}.

Despite the fact that winds in HMXBs may be very different from those in isolated, massive stars, the density distribution based upon the β-law (Eq. 6) has been used as a convenient model. For example, Lewis et al. (1992) were able to model *Ginga* spectra of Vela X-1 using a Monte Carlo simulation of fluorescence and scattering in a wind model for which β was set to 0.5 at distances greater than $0.3R_\star$. Closer to the stellar surface, a modification of the wind structure, an exponential form with scale height $\sim 0.1R_\star$ as proposed by Clark, Minato, & Mi (1988) for Cen X-3, was necessary to explain the gradual eclipse transitions. The physical processes of X-ray scattering and absorption are often sufficient to describe the spectra seen with low-resolution detectors. However, an *ASCA* observation of Vela X-1 over an eclipse (Nagase et al. 1994) was dominated by recombination emission lines. We describe in the next section a method for calculating emission line spectra for model winds.

4.2.   The DEM Approach

When recombination is the dominant line production mechanism, the line power can be written as

$$P_{\text{line}}(\xi) = \frac{n_{\text{H}}}{n_{\text{e}}}\ AF_{i+1}(\xi)\alpha_{\text{eff}}(\xi)\ E_{\text{line}}, \qquad (11)$$

where F_{i+1} is the ionic fraction of the recombining ion. Recombination lines can be associated with particular values of ξ—each line can be assigned a ξ *of formation* ξ_{f}. These occur at the value of ξ for which $P_{\text{line}}(\xi)$ is a maximum, equivalent to maximizing $F_{i+1}(\xi)\alpha_{\text{eff}}(\xi)$. The *ASCA* eclipse spectrum of Vela X-1, for example, included emission from Ne IX for which $\log\xi_{\text{f}} = 1.8$, as well as Fe XXVI, for which $\log\xi_{\text{f}} = 3.6$. The presence of bright emission lines from species of such disparate ξ_{f} suggests that the reprocessing gas in Vela X-1 is composed of a non-trivial distribution in ξ. This comes as no great surprise, based upon the discussion in the previous section, to the extent that the simple model described there is a reasonable representation of the true matter distribution.

To a first approximation, we can write $L_{\text{line}} = P_{\text{line}}(\xi_{\text{f}})EM_{i+1}(\xi_{\text{f}})$ where $EM_{i+1} = n_{\text{e}}^2 V_{i+1}$ is called the *volume emission measure*. Without corollary information that would allow an independent determination of either the density or the emission volume, we can describe the "amount" of gas only in terms of the emission measure. It is thus natural to plot the set $EM_{i+1}(\xi_{\text{f}})$ vs. ξ_{f}, with each charge state represented by a point (Sako et al. 1999). Dividing each $EM_{i+1}(\xi_{\text{f}})$ by the width $\Delta\log\xi$, an estimate of the width of $P(\xi)$, gives an approximation to the differential emission measure (DEM) distribution, the emission measure per unit $\log\xi$, which is defined more formally below. The significance of this is that the empirical DEM distribution is relatively easy to construct, and can be compared to theoretical predictions derived from geometrical models of the source. This has an advantage over comparisons of spectra, since large-scale models of XRBs often use highly schematic atomic models. It is well-known, however,

that recombination emission, especially from H-like ions, is efficient over a wide range in ξ (Hirano et al. 1987; Ebisawa et al. 1996). Therefore, constructing an empirical DEM distribution in this way leaves us with, at best, a crude approximation of the true, continuous DEM distribution. With a geometrical model of the system, we can improve upon this situation.

Electron scattering and fluorescence emissivities are proportional to $n_{\mathrm{e}}L/r^2$ and $n_{i-1}L/r^2$, respectively. Therefore, by substituting $n\xi$ for L/r^2, we see that the emissivities for scattering and fluorescence can, just as for recombination lines, be written as n_{e}^2 times some function of ξ, which we denote by P and call the radiative power, a generalization of the line power discussed above.

From the definition of the volume emission measure $EM = \int dV\, n_{\mathrm{e}}^2$, we define the function $EM(\xi, v_\parallel)$ by limiting the volume of integration to regions for which the ionization parameter ξ' is less than the value ξ and for which the radial velocity $v_\parallel'$ is less than the value $v_\parallel$. The monochromatic luminosity of a photoionized gas distribution is then:

$$L_\nu = \int d\log\xi \int dv_\parallel \left[\frac{\partial^2 EM(\xi, v_\parallel)}{\partial \log\xi \, \partial v_\parallel} \right] P_\nu(\xi). \qquad (12)$$

With low to moderate resolving power, the Doppler broadening and shifts of lines due to motion of the wind are usually not detectable, and the $v_\parallel$ dimension in Eq. (12) is collapsed. That is, we define $EM(\xi)$ by limiting the volume of integration to the region with $\xi' < \xi$, so that

$$L_\nu = \int d\log\xi \left[\frac{dEM(\xi)}{d\log\xi} \right] P_\nu(\xi). \qquad (13)$$

The quantities in brackets in Eqs (12) and (13) are DEM distributions. The one-dimensional version is the only one that has seen use so far.

When calculating a large number of spectra, where each is based upon a particular DEM distribution, this representation, which splits the spatial and spectral components of local spectra, is computationally efficient. First, for a given ionizing radiation spectrum and chemical abundance set, a library of $P_\nu(\xi)$ on a ξ-grid is compiled. Then, for each wind model, the DEM distribution is computed by summing the emission measure in spatial cells into bins of $\log\xi$. For a stellar wind which is spherically symmetric, ξ and n_{e} are symmetric about the line of centers, and this symmetry significantly reduces the load of computing the DEM distribution. Where the wind models differ only by the luminosity of the X-ray source or by an overall scaling, additional computational efficiency is afforded, as the DEM distribution is changed only by shifts along the $\log\xi$ axis or by changes in the overall normalization, and it is not necessary to repeat the summation over spatial cells (Wojdowski et al. 2000).

4.3. Applications

The DEM distribution for a radiatively driven wind depends not only on the parameters of the wind ($\dot{M}$, v_∞, and β) and the luminosity of the X-ray source L_{x}, but also on the companion star radius $R_\star$ and the orbital separation a. (Note that the dependence on a is "hidden" in Eq. (9) through the relation

between r and R.) Furthermore, the part of the wind which is occulted at a given orbital phase depends on the orbital inclination i. In HMXBs where the compact object is a pulsar that is eclipsed during its orbit, $R_\star$, a, and i can be determined precisely using Doppler pulse delays, Doppler shifts of optical lines from the companion star, and the X-ray eclipse duration. Furthermore, if the distance to the system is known, L_x may also be constrained from the uneclipsed flux.

Taking advantage of the fact that the system parameters of Vela X-1 are well constrained, Sako et al. (1999) computed DEM distributions for a set of wind models, assuming that the β-law is valid. Emission spectra for these DEM distributions were calculated as described above, and compared to the eclipse *ASCA* spectrum. They found values of β (0.79) and $\dot{M}$ (2.7×10^{-7} $M_\odot$ yr^{-1}) that provided an accurate reproduction of the recombination line spectrum. It is interesting to compare, as a consistency check, the estimate of $\dot{M}$ that one would obtain from Eq. (10). The value of ξ_0, using a plot of $EM(\xi_\mathrm{f})$ vs. ξ_f, as discussed in §4.2, can be estimated to be $\sim$ 500-1000. From Eq. (10), this gives $\dot{M} \sim$ 2.6-5.2 $\times 10^{-7}$ $M_\odot$ yr^{-1}, in remarkably good agreement with the result based upon more detailed considerations.

The wind model used by Sako et al. does not, however, predict fluorescent emission from low charge states, which are observed in Vela X-1 at all orbital phases. In order to obtain a good fit to the data, a set of features were added to the fitting program to accommodate lines from near-neutral Mg, Si, S, Ar, Ca, Fe, and Ni. A related problem is that the highly-ionized wind model does not account for the intrinsic near-neutral column density needed to attenuate the continuum flux. Finally, and perhaps most glaringly, the derived $\dot{M}$ is an order of magnitude smaller than the value derived from earlier studies (Dupree et al. 1980; Sato et al. 1986), and considerably smaller than expectations based upon wind mass loss rates from isolated early-type stars. The problem can be summarized as follows: (1) the explanation of recombination emission from K-shell ions requires a certain range of ξ and a certain range of DEM magnitudes, which leads to small $\dot{M}$; (2) a model using a larger value of $\dot{M}$, while explaining the column density variation, X-ray fluorescence, and UV evidence of low charge states, predicts that the recombination line zones would closely surround the neutron star, with dimensions so small that they would be occulted by the companion star during eclipse.

Sako et al. showed that by abandoning the assumption that the wind is smooth, this apparent discrepancy could be reconciled (cf., Nagase et al. 1983; Sato et al. 1986). A picture of the wind arises for which $\sim$ 90% of the wind's mass is in the form of cool, dense clumps, but $\sim$ 95% of the irradiated wind volume within the binary system conforms to the simple β-law/Hatchett-McCray model used to fit the recombination emission. This picture is able to bring the X-ray recombination spectrum, the fluorescent line spectrum, the intrinsic column density, and the presence of the low charge states observed in the UV into accord, and yields an estimate of the total mass loss rate ($\dot{M}_\mathrm{tot} \sim 2 \times 10^{-6}$ $M_\odot$ yr^{-1}) that agrees well with earlier numbers. Finally, this clumpiness may be related to short-term variability (10^3-10^4 s) in the X-ray luminosity through collisions of dense wind structures with the neutron star.

In hot star winds, clumping is expected on theoretical grounds, and is evidenced by the appearance of so-called "discrete absorption components" (DACs) in UV line profiles. On a timescale of a few days, DACs may appear in the absorption trough of a UV P Cygni profile, which subsequently begin to narrow and move to the blue (e.g., Kaper et al. 1996). X rays are observed from isolated O and B stars (e.g., Seward et al. 1979), whose origin has been attributed to shocks in radiatively driven winds (Lucy 1982). Line-driven stellar winds are subject to several instabilities (MacGregor, Hartmann, & Raymond 1979; Lucy & White 1980; Owocki & Rybicki 1984), such as the Rayleigh-Taylor instability, which will produce clumps with sizes $\sim 10^{11}$ cm (Carlberg 1980). Thus it is not entirely surprising that a clumpy wind is invoked to explain the X-ray spectrum of Vela X-1. The relation between clumping in a normal wind and clumping in an X-ray irradiated wind is not established, however. While the characteristics of the clumps in the model are reasonable, they are more or less *ad hoc*, do not explain their origin or survivability, and do not accommodate a clump population that is likely to possess a distribution of sizes and densities.

Liedahl et al. (2000) speculate that the clumped component of the wind, since it is characterized by small values of ξ, has sufficient opacity to the companion's UV field to permit normal radiative driving. While the diffuse wind is too highly ionized to be driven by UV radiation, the clumps, which contain most of the wind mass, may mediate the transfer of momentum to the outflow, with the result that the hotter, diffuse wind is "pushed" outward, thereby imparting the β-law velocity distribution to the recombination emission line regions. Alternatively, the hotter, more tenuous wind component may originate from the evaporation of material off the clump surfaces, which then leaves it tied to the clump velocity distribution.

Wojdowski et al. (2001) applied a similar DEM analysis of the *ASCA* spectrum of Cen X-3. Unlike Vela X-1, for which a wind terminal velocity has been measured (Dupree et al. 1980), v_∞ for Cen X-3 is not known. From Eq. (7) it can be seen that the local density, hence DEM, scales with $\dot{M}/v_\infty$. Thus the ratio $\dot{M}/v_\infty$ must be used as a fitting parameter, rather than $\dot{M}$. Also by contrast to Vela X-1, it is already known that any clump population should have a negligible effect on the Cen X-3 X-ray spectrum, as evidenced by the near constancy with orbital phase of the equivalent width of the fluorescent iron Kα complex (Ebisawa et al. 1996). In other words, were the wind highly clumped and extended, a dramatic increase in the Fe Kα equivalent width would accompany eclipse of the compact X-ray source. Vela X-1, for example, *does* show a large-amplitude variability in the Fe Kα equivalent width (Sato et al. 1986). Therefore, it is assumed from the outset that the wind in Cen X-3 is smooth, and that, for a given v_∞, the best-fit $\dot{M}$ pertains to the total mass-loss rate of the companion.

The value of $\dot{M}/v_\infty$ derived from the Wojdowski et al. analysis of the *ASCA* Cen X-3 spectrum is 1.6×10^{-9} M$_\odot$ yr^{-1} (km s^{-1})$^{-1}$, which is comparable to that obtained for isolated stars of similar spectral class. It is also comparable to the value found for Vela X-1, if the clumped component's contribution to $\dot{M}$ is included. While the wind mass loss rates in Cen X-3 and Vela X-1 may be similar, the characters of the winds are quite different. This is demonstrated by Fig. (2), which shows a comparison of the DEM distributions obtained from fits

to the *ASCA* data. The apparent difference in the total emission measures (the integrals of the DEM distributions) is not real, and results simply from the omission of the DEM distribution for the (off-scale) lower-ξ region. Indeed, the total emission measure in a spherically symmetric wind is $EM \sim (\dot{M}/v_\infty)^2/m_{\mathrm{p}}^2 R_\star$, in which a substantial difference between the two systems is not to be found. A reliable calculation of the distribution for $\log\xi < 1.5$ would require a thorough analysis of the line complexes from fluorescing material, which is impossible without much higher spectral resolving power. Above $\log\xi = 1.5$, however, the difference between the two curves is real. The relatively small DEM magnitudes in Vela X-1 reflect the fact that most of the wind mass is "locked up" in dense clumps.

It is well known that X-ray irradiated gas is prey to thermal instabilities near the range of ionization parameter relevant to X-ray recombination line emission (see §5.5). In this context the dimensionless *pressure ionization parameter* ($\Xi = L/4\pi r^2 nkTc$ for a point X-ray source) is more useful than ξ, which is sometimes called the *density ionization parameter*. The instability criterion is given by $d\ln T/d\ln\Xi < 0$, often satisfied for a range of Ξ in X-ray photoionized gases, depending on the spectral shape function. Inside this range ($-1 \lesssim \log\Xi \lesssim 1$; Krolik, McKee, & Tarter 1981), both a dense, cool phase and a hot, tenuous phase may coexist (i.e., there are two values of ξ for a given Ξ in this range). To estimate Ξ for winds in HMXBs, we use the continuity equation (Eq. 7) to substitute for n in the definition of Ξ, which gives

$$\Xi = \frac{\mu m_{\mathrm{p}} L v_\infty}{kT\dot{M}c} \left(\frac{R}{r}\right)^2 \left(1 - \frac{R_\star}{r}\right)^\beta. \tag{14}$$

As we did earlier for ξ, we can define a characteristic value of Ξ according to

$$\Xi_0 = \frac{\mu m_{\mathrm{p}} L}{kTc\,(\dot{M}/v_\infty)} = 0.9\,\frac{L_{36}}{T_6\,(\dot{M}/v_\infty)_{-9}}, \tag{15}$$

where L is given as a multiple of 10^{36} erg s^{-1}, T as a multiple of 10^6 K, and $\dot{M}/v_\infty$ as a multiple of 10^{-9} M$_\odot$ yr^{-1} (km s^{-1})$^{-1}$. For Vela X-1, with $(\dot{M}/v_\infty)_{-9} = 1.2$ for the total mass loss rate, and $T_6 \approx 1$, we find $\log\Xi_0 = 0.5$, which is consistent with the two-phase gas, possibly explaining the clumping. For Cen X-3, with its much higher X-ray luminosity, we find $\log\Xi_0 = 1.8$, above the range of Ξ for which the thermal instability applies—no cool phase is allowed. This is a crude argument, but it is consistent with the X-ray spectra, and suggests that further work into the formation and survivability of clumped winds in HMXBs may show that thermal instabilities play an important role.

4.4. Physical Simulations

The interplay of the various physical processes in HMXB winds is complex, and computational simulations that include hydrodynamics, the effects of radiation on the thermal balance, and gravitational and non-inertial forces are necessary to determine the resulting structure and kinematics. As these simulations are necessarily inexact, it is desirable to test them by predicting how these simulated wind models would appear when observed with real observatories and comparing these predictions with observational data. In principle, simulations
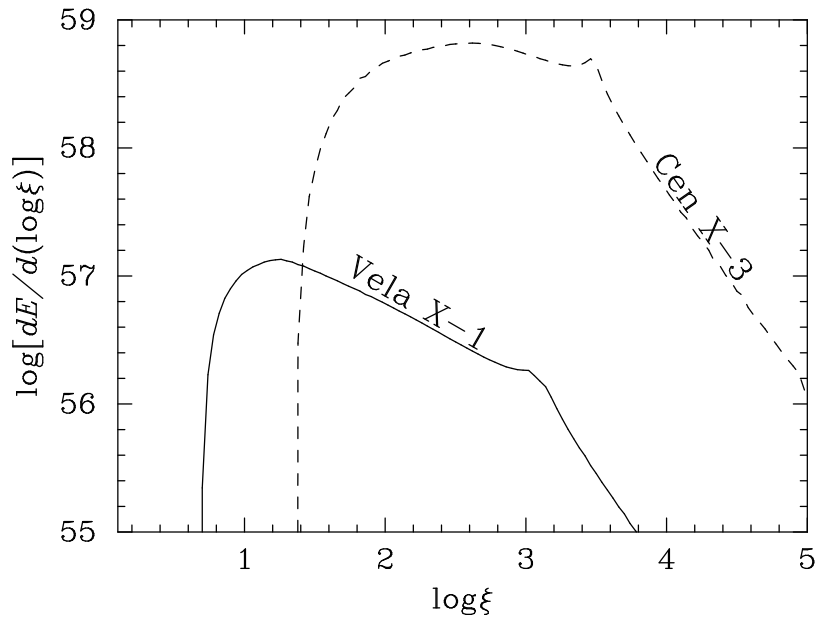
Figure 2. Differential emission measure distributions of Vela X-1 (Sako et al. 1999) and Cen X-3 (Wojdowski et al. 2001). For Vela X-1, the contribution from low-ξ fluorescing material, which would cause an upturn in the DEM curve moving to lower ξ, is not included. The substantial difference in the DEM magnitudes for $\log \xi > 1.5$ illustrates the distinction between a smooth wind (Cen X-3) and a clumped wind (Vela X-1). The vertical axis is scaled in units of cm^{-3}.

could be improved by comparing predicted spectra to observed spectra, identifying the physical processes which need to be treated in greater detail in order to reproduce the observed spectra, and then iterating. This is not generally practical, however. Running a simulation of the wind for even a single set of assumptions and approximations takes a large amount of computer time and performing a large number of iterations of simulating and comparing to observation is generally impossible. Furthermore, if a simulation compares unfavorably to observational data, it may be unclear exactly how to change the simulation in order to reproduce the observations. Our method of using simple velocity and density distributions, therefore, serves as a complement to more computationally intensive calculations, testing approximate wind densities and geometries to inform simulations.

Two-dimensional simulations of gravitational accretion from a smooth flow onto a compact object using an adiabatic equation of state have shown that this process is time variable and results in shocks (Fryxell & Taam 1988; Taam & Fryxell 1989). A series of simulations has considered the effect of X-ray ionization on the wind from the OB companion. Blondin et al. (1990) conducted two dimensional simulations of accretion from a wind, including disruption of the radiative driving by X-ray ionization of the wind, which showed the formation of accretion wakes persisting over a significant fraction of the system size. They suggest that the dense gas at the boundary of the accretion wake could account for phase-dependent absorption features seen from HMXBs. Blondin (1994) simulated HMXBs with large X-ray luminosities, including the driving of a thermal wind from the X-ray irradiated face of the companion star. Only a few attempts have been made to compare simulations with observational data quantitatively. One reason is that many simulations are done in two dimensions and the quantitative extrapolation of the results to three dimensions is not straightforward.

The wind in SMC X-1 was simulated by Blondin & Woo (1995) in three dimensions, including UV radiation driving and its disruption by X-ray ionization, and also the driving of a thermal wind from the X-ray heated face of the companion. This simulation included the gravity of the supergiant companion and non-inertial forces but not the gravity of the compact object. The electron scattering and fluorescence spectra from this simulation were calculated, and compared to *Ginga* spectra by Woo et al. (1995). The simulation was able to reproduce the observed scattered continuum, as well as the extended eclipse transition. Wojdowski et al. (2000) observed SMC X-1 with *ASCA* over an eclipse, and computed the scattering, fluorescence, and recombination from the simulation. The observed spectrum had no obvious emission features. This excluded the possibility that the DEM distribution of the wind contained a large component with $1 < \log \xi < 3$, as strong recombination emission features (predominantly O VII and O VIII) are emitted below 2 keV at those ionization parameters. In the simulation, the wind was denser in the X-ray shadowed region, but dense finger-like structures from the shadowed side of the companion extended into the X-ray illuminated side. These structures were characterized by ionization parameters in the range $1 < \log \xi < 3$, and their integrated emission measure was greater than that allowed by the observed spectrum by an order of magnitude. It was therefore concluded that the finger-like structures could not exist as they appeared in the simulation. Again, it is not clear how

the physical assumptions of this simulation should be changed in order to make the resultant wind conform to observations.

Despite the growing sophistication of these simulations, there are still potentially important physical effects that have not been accounted for. For example, none of the simulations mentioned above properly account for the transfer of X rays through the wind. To take an example, the inclusion of detailed X-ray transfer may result in the formation of Strömgren ionization boundaries around the X-ray source. Outside of the Strömgren surface, the wind is not highly ionized, thus UV radiation driving is not strongly affected by the X-ray field of the compact object (Masai 1984).

4.5. High-Resolution Spectroscopy and X-ray Line Profiles

The high spectral resolving power of *Chandra* and *XMM* bring the possibility of resolving line profiles. Line widths of order 1000 km s^{-1} have already been observed with *Chandra* in Cir X-1 (Brandt & Schulz 2000) and Cyg X-3 (Paerels et al. 2000). The canonical HMXB systems Cen X-3 and Vela X-1, however, show emission lines with widths consistent with zero, i.e., no broader than a few 100 km s^{-1} (Wojdowski et al. 2001; N. Schulz, priv. comm.). For comparison, it is interesting to note that X-ray line widths in isolated O and B type stars are as large as $\sim$ 1000 km s^{-1} (Kahn et al. 2001; Schulz et al. 2000; Waldron & Casinelli 2000). This suggests one or both of the following possibilities: (1) X-ray ionization slows the companion star wind in HMXBs; (2) X-ray line emission from HMXBs traces a different, lower velocity part of the wind than in isolated stars.

To illustrate the second possibility above, Fig. (3) shows the emissivity contours of two lines, as calculated using the wind model of Sako et al. (1999). The emissivities, which include the n_e^2 weighting, are by far the largest nearest the companion star, in what for an isolated star would be the acceleration zone, where the velocity is relatively low. This primarily shows that outflowing material on the irradiated side of the companion is ionized to high levels by the X-ray field long before the wind attains a high velocity. Owing to this effect, X-ray emission line profiles may often be fairly insensitive to wind velocity profiles. It remains a puzzle as to why the X-ray emitting plasma in the Wolf-Rayet XRB system Cyg X-3 shows such large velocity widths.

When X-ray line optical depths are small, emission line widths and shifts may be calculated by the methods described in the previous section. However, to simulate situations where absorption is important (for example, systems in which P Cygni lines have been observed) modifications must be made. The emission spectrum for a given spatial cell of gas can still be treated as though it were function of ξ alone, but, in order to compute the total spectrum, absorption along the line of sight to the observer must be applied to each cell (see Wojdowski et al. 2000).

The *Chandra* X-ray spectrum of Circinus X-1 shows H-like and He-like lines from Ne, Mg, Si, S, and Fe, with line widths of $\sim$ 2000 km s^{-1} and P Cygni profiles, the first observed in the X-ray band, indicative of an accelerating outflow with a comparable velocity (Brandt & Schulz 2000). Interestingly, optical observations suggest that Cir X-1 is a low-mass system (Glass 1994), which is also implied by its X-ray spectrum and variability (Shirey, Bradt, & Levine 1999),
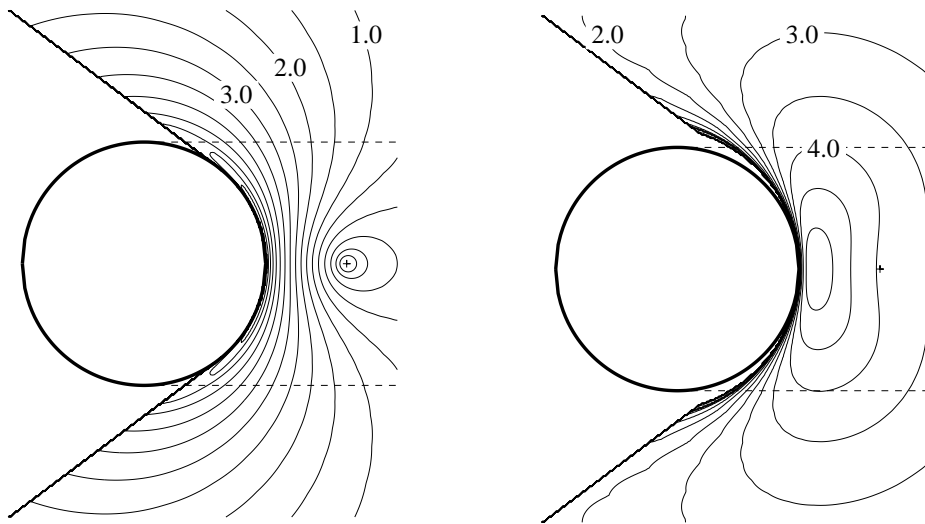
Figure 3.   Contour plots of the common logarithm of the line emis-
sivities (in $\mathrm{ph\,cm^{-3}\,s^{-1}}$) of Si XIII (*left*) and Fe XXVI (*right*) assuming
the Vela X-1 wind model used by Sako et al. (1999). Position of the
X-ray source is indicated by a + sign. Dashed lines delineate the part
of the stellar wind occulted by the companion star at orbital phase
0.0. Diagonal lines tangent to the companion delineate the shadow
cone. Contours show the weighting of the line luminosities toward low-
velocity regions near the companion star.

as well as its Type I X-ray bursts (Tennant, Fabian, & Shafer 1986). Thus the X-ray continuum is thought to be viewed through an accretion disk wind, which in some ways poses an even greater challenge for modelers than stellar winds; for example, conditions at the base of the wind vary with disk radius. In order to obtain the values of ξ corresponding to the observed ionic species, a density $n > 10^{14}$ cm^{-3} is required. This is consistent with the model values for the atmospheric density in a hydrostatic disk (see §5). In addition, a broad (~ 2000 km s^{-1}), blueshifted Hα line may indicate an outflow of an optically thick gas, indicative of even larger densities, perhaps at the base of the wind (Johnston, Fender, & Wu 1999). A model spectrum of this source is not yet available, but dynamic radiation-driven accretion disk wind models have been made for AGN parameters (Proga, Stone, & Kallman 2000).

Here we leave the topic of winds behind. In the following sections, we outline some of the basic issues relating to ("windless") accretion disk structure, but note here that in some situations, such as that exemplified by Cir X-1, the physics of irradiated winds and the physics of irradiated accretion disks cannot be so neatly separated.

5.   X-Ray Spectroscopy of Accretion Disks in LMXBs

The intense emission from LMXBs is attributed to the efficient conversion of gravitational potential energy into radiation, as mass is transferred from an otherwise normal star to a compact object (Shklovsky 1967). The mass donor (companion) overflows its Roche lobe, thereby spilling matter through the inner Lagrangian point (L1). Born with large angular momentum in the co-rotating frame, the accreting matter follows trajectories that cannot directly intersect the compact object. Instead, a disk forms, and a tangential viscosity forces the disk material to spiral in (Prendergast & Burbidge 1968).

Shakura & Sunyaev (1973; SS73, hereafter) derived an analytic model of radiatively efficient matter infall in a disk geometry. The viscously dissipated energy is assumed to be locally radiated as blackbody emission. The UV continuum of cataclysmic variables is in rough agreement with the above assumption (Kiplinger 1979; Pringle, Verbunt, & Wade 1986; Wade 1984). The SS73 parameterization of the viscosity η in terms of the total pressure P, such that $\eta = \alpha P$, where α is a constant, provides a zeroth order picture of the disk, but it is likely incorrect in detail. Numerical magnetohydrodynamic (MHD) models (see J. Stone article in this issue) show that α varies by a few orders of magnitude throughout the disk, but that on average its value ranges from $\sim 10^{-3}$–10^{-1}. Nevertheless, the α-disk model is one of the simplest and most useful of its kind, especially since many results do not sensitively depend on the value of α. Comparisons of the α-disk model with observations of XRBs and AGN are presented in Frank, King, & Raine (1992) and Malkan (1983), respectively. Modern accretion flow models, of which the α-disk is a subset, are described by Chen et al. (1995).

The viscous mechanism in accretion disks allows accretion to occur by transporting angular momentum outward, matter inwards, and by dissipating gravitational energy into heat inside the disk. The viscosity mechanism has been

identified in theory as a magneto-rotational instability due to the entanglement of magnetic fields from the differential rotation of gas in Keplerian orbits, akin to a dynamo effect (Balbus & Hawley 1998). In MHD models, this mechanism provides the energy dissipation and angular momentum transfer needed to naturally produce mass accretion with self-sustained magnetic fields B that are much smaller than the equipartition level ($B^2/8\pi \ll \rho v^2$), where ρ is the gas density and v is the thermal velocity.

The optically thick α-disk model has been accepted with only a few modifications since its inception (Abramowicz et al. 1988; Chen & Taam 1993; Luo & Liang 1998), and a significant fraction of the X-ray continuum in LMXB is interpreted as thermal emission from the disk. Yet, the presence of non-thermal continuum radiation in all of these sources and line emission from highly-ionized atomic species in many of them is not accommodated by the standard α-disk model. Moreover, neutron star or coronal thermal emission has made the discernment of disk continuum emission ambiguous. As such, X-ray line emission is a potentially powerful tool for elucidating the properties of accretion disks.

5.1.   Observations

With the exception of Fe K emission in the 6.4–7.0 keV range, discerning X-ray line emission in LMXBs has been challenging, owing to limitations in sensitivity and spectral resolving power, as well as the difficulties associated with attempts to extract line emission from data dominated by intense continuum emission. Still, measurements obtained with the *Einstein* Objective Grating Spectrometer (Vrtilek et al. 1991), the *ROSAT* Position Sensitive Proportional Counter (Schulz 1999), and the *ASCA* CCD imaging detectors (Asai et al. 2000) have shown that the spectra of a large fraction of bright LMXBs exhibit line emission.

The X-ray line emission arises presumably as the result of irradiation of the disk by the X-ray continuum, producing an extended source of reprocessed emission. Evidence of X-ray emission from extended regions in LMXBs comes from the spectral variations during ingress and egress phases of eclipses, and during rapid intensity fluctuations known as dips. Dips are thought to result from variable obscuration and attenuation of the primary continuum by material near the outer disk edge, which has been thickened due to impact of the accretion stream with the disk (White & Holt 1982; cf., Frank, King, & Lasota 1987). Hard X-ray emission, presumably originating in an accretion disk corona (ADC), and representing a few percent of the non-eclipse flux, remains during mid-eclipse in several LMXB, implying that the ADC is larger than the secondary star (White & Holt 1982; McClintock et al. 1982). LMXB spectra during eclipses or dips may harden or soften. Most sources harden during dips (Parmar et al. 1986), consistent with photoelectric absorption, but there are exceptions like the softening of X1624-490 (Church & Balucinska-Church 1995), and an unchanging X1755-338 (White et al. 1984; Church & Baluncinska-Church 1993). Sources such as X0748-676, X1916-053, and X1254-690 show evidence for an unabsorbed spectral component (Parmar et al. 1986; Church et al. 1997) during dips, revealing an extended source of X rays which is larger than the ADC. These soft X rays are likely radiation reprocessed in the accretion disk. Dip ingress/egress times indicate ADC sizes in the 10^9–5×10^{10} cm range, a factor

of a few smaller than the accretion disk sizes calculated from typical orbital parameters (Church 2000 and references therein).

The increasing availability of high-resolution X-ray spectra from XRBs, thanks to *Chandra* and *XMM-Newton*, makes possible the application of detailed line diagnostics, such as density-sensitive line ratios and line profiles. Currently, however, only a few LMXB spectra from these observatories are available. Of these, a 100 ks observation of X0748-67 using the Reflection Grating Spectrometer (RGS) shows the richest line spectrum (Cottam et al. 2000; Fig. 5) and, therefore, provides a useful testbed for accretion disk atmosphere models. System parameters of X0748-67 other than the orbital period (3.82 hr) and inclination (75-82°) are unknown (Parmar et al. 1986). The RGS lightcurve shows factor-of-10 fluctuations in flux, plus several Type I X-ray bursts with the exponentially decaying flux expected from a nuclear detonation on the surface of a neutron star. No correlation of the flux variability with orbital phase was observed. Excluding the burst phases, spectra at low and high states were added for comparison. The high state shows O VIII Lyα ($1s - 2p_{1/2,3/2}$), O VII Heα ($n = 2 \rightarrow n = 1$; see §2.1), and Ne X Lyα line emission, with O VII and O VIII absorption edges. The low state spectrum shows even more lines but no edges, with the continuum emission absent. Emission from O VII and O VIII RRC can then be detected, as well as Ne IX Heα and N VII Lyα. The strongest line, O VIII Lyα, is broader than the expected line spread function, with a width of $\sigma = 1390 \pm 80$ km/s. Upper limits for the O VII and Ne IX R ratios indicate a density $n_e > 7 \times 10^{12}$ cm^{-3}. The line ratio $G > 4$, consistent with a purely photoionized plasma. Unlike the hard X-ray flux, the RGS count rate does not change during eclipses, which is indicative of an extended source.

5.2. Radiatively Heated Accretion Disks

In LMXB roughly half of the gravitational potential energy is released in the vicinity of the compact object (i.e., in accretion shocks near the neutron star surface). The flared disk is exposed to this radiation, and will be heated by it. In fact, radiative heating can exceed internal viscous heating in the outer region of the disk. The temperature structure of the disk can thus be controlled by the X-ray field, photoionizing the gas, suppressing convection, and increasing the scale height of the disk. Photoionization in the disk is balanced by recombination, which produces line emission.

Assuming that all the viscous heating and radiative heating from illumination by the central source is radiated locally as a blackbody (as in the SS73 model), Vrtilek et al. 1990 find, for a geometrically thin disk, and for $r \gg R_1$, where R_1 is the radius of the compact X-ray source,

$$\sigma T_{\text{phot}}^4 \simeq \frac{3GM_1\dot{M}}{8\pi r^3} + \frac{(1-\eta)L_{\text{x}}\sin\theta(r)}{4\pi r^2}, \qquad (16)$$

where T_{phot} is the photospheric temperature, M_1 is the mass of the compact X-ray source, θ is the grazing angle of the incident X-ray flux with respect to the disk surface, and η is the X-ray "albedo," such that $1 - \eta$ is the fraction of X rays absorbed at the photosphere. The second term on the right-hand side of

Eq. (16) will be the dominant one when

$$r > 2.3 \times 10^8 \left(\frac{M_1}{M_\odot}\right) \left(\frac{1-\eta}{0.1}\right)^{-1} \left(\frac{\sin\theta}{0.1}\right)^{-1} \left(\frac{\epsilon_x}{0.1}\right)^{-1} \text{ cm,} \qquad (17)$$

where we have written the X-ray luminosity in terms of an "X-ray accretion efficiency" ϵ_x, according to $L_x = \epsilon_x \dot{M} c^2$. For example, accretion onto a neutron star results in roughly $1/2$ of the gravitational potential energy being converted into X rays, or $\epsilon_x = GM_1/2c^2 R_1$. The disk, therefore, is radially divided into an inner region dominated by internal dissipation, and an outer region dominated by external illumination. External radiation will dominate the disk atmosphere energetics for the outer two or three decades in radii, and the local dissipation and magnetic flare heating, if any, can be ignored there.

5.3.   Vertical Structure

To obtain a high-resolution spectrum of an accretion disk, and in particular one for which the outer layers are X-ray photoionized, several authors have calculated the vertical structure by solving the radiation transfer equations, assuming hydrostatic equilibrium. Models have been applied to AGN and LMXB in the high-L_x state, since in the low-state other accretion modes ensue. The radiative transfer is typically simplified by using an on-the spot approximation and the escape probability formalism. Due to photoelectric absorption and Compton scattering, the ionization structure of the disk turns out to be stratified, approximated by a set of zones, each with a single ionization parameter. The ionization structure of the disk can be solved by using photoionization codes, such as CLOUDY and XSTAR, to calculate the ionization and thermal equilibrium state of the gas at each zone.

Ko & Kallman (1991; 1994) calculated the vertical structure of an illuminated accretion disk and obtained the recombination X-ray spectrum for individual rings on the disk. Raymond (1993) utilized the calculated temperatures in Vrtilek et al. (1990) to calculate a vertical structure and the UV spectrum from the global structure of the disk. Both assumed parameters for LMXBs, and gas pressure-dominated disks. Later models of photoionized accretion disks focused primarily on calculating the Fe Kα fluorescence emission from AGN disks.

Rozanska & Czerny (1996) modeled semi-analytically the stratified, photoionized transition region between the corona and the disk. They found that their approximations, which included on-the-spot absorption, matched more accurate radiation transfer codes, including optically thick scattering, for optical depths $\lesssim 10$. They also discussed the existence of a two-phase medium, stopping short, however, of calculating an X-ray line spectrum. Nayakshin, Kazanas, & Kallman (2000) modeled a radiation-pressure dominated disk and showed that the vertical structure of the disk implied significant differences in the Fe K fluorescence line spectrum compared to that predicted by constant-density disk models (e.g., Ross & Fabian 1993; Matt, Fabian, & Ross 1993; Zycki et al. 1994). In addition, Nayakshin, Kazanas, & Kallman (2000) found that the gas was thermally unstable at certain ionization parameters, which created an ambiguity in choosing solutions, and a sharp transition in temperature in the disk.

Using the Raymond (1993) photoionization code, we have calculated the disk atmosphere structure of each annulus by integrating the hydrostatic balance

and 1-D radiation transfer equations for a slab geometry:

$$\frac{\partial P}{\partial z} = -\frac{GM_1 \rho z}{r^3} \tag{18}$$

$$\frac{\partial F_\nu}{\partial z} = -\frac{\kappa_\nu F_\nu}{\sin \theta} \tag{19}$$

$$\frac{\partial F_\nu^{\mathrm{d}}}{\partial z} = -\kappa_\nu F_\nu^{\mathrm{d}} \tag{20}$$

where P is the pressure, ρ is the density, F_ν is the incident radiation field, F_ν^d is the reprocessed radiation propagating down towards the disk midplane, z the vertical distance from the midplane, θ the grazing angle of the radiation on the disk, κ_ν is the local absorption coefficient. To these equations is added the further constraint that local thermal equilibrium is satisfied:

$$\Lambda(P, \rho, F_\nu) = 0 \tag{21}$$

The difference between heating and cooling Λ includes Compton scattering, bremsstrahlung cooling, photoionization heating, collisional line cooling, and recombination cooling from H, He, C, N, O, Ne, Mg, Si, S, Ar, Ca, and Fe ions. Equations (18)–(20) are integrated simultaneously using a Runge-Kutta method with an adaptive stepsize control routine with error estimation, and Eq. (21) is solved by a globally convergent Newton's method (Press 1994). At the height z_{cor} ("cor" for "corona"), the equilibrium T is close to the Compton temperature, from which we begin to integrate downward until $T < T_{\mathrm{phot}}(r)$. The optically thick part of the disk, with temperature T_{phot}, is assumed to be vertically isothermal (Vrtilek et al. 1990). We get T_{phot} from Eq. (16).

The boundary conditions at z_{cor} are set to

$$P(z_{\mathrm{cor}}) = \rho_{\mathrm{cor}} k T_{\mathrm{compton}} / \mu m_{\mathrm{p}} \tag{22}$$

$$F_{\mathrm{x}}(z_{\mathrm{cor}}) = L_{\mathrm{x}} / 4\pi r^2 \tag{23}$$

$$F_\nu^{\mathrm{d}}(z_{\mathrm{cor}}) = 0 \tag{24}$$

where $F_{\mathrm{x}} \equiv \int F_v \, d\nu$, and μ is the average particle mass in units of the proton mass m_{p}. The boundary conditions at z_{phot} for F_ν and F_ν^{d} are set free, and we use the shooting method (Press 1994) with shooting parameter ρ_{cor}, adjusted until $P(z_{\mathrm{phot}}) = \rho_{\mathrm{phot}} k T_{\mathrm{phot}} / \mu m_{\mathrm{p}}$ at the photosphere. Note ρ_{phot} is the α-dependent density calculated for a standard SS73 disk.

An important feature of this model is that we allow the incident radiation to modify the disk atmosphere geometry, such that the heating and expansion of the atmosphere resulting from illumination are used to calculate the height profile of the atmosphere as a function of radius. The atmospheric height is used to derive the input grazing angle of the radiation for the next model iteration. This contrasts with calculating the grazing angle using the pressure scale height of the optically thick disk (Vrtilek et al. 1990), which is in general well below the photoionized atmosphere, and which underestimates the grazing angle and

the line intensities by an order of magnitude. To get T_{phot} self-consistently from Eq. (16), we need to find $\theta(r)$ using

$$\theta(r) = \arctan(dz_{\text{atm}}/dr) - \arctan(z_{\text{atm}}/r) \qquad (25)$$

where $z_{\text{atm}}(r)$ is defined as the height where the frequency-integrated grazing flux is attenuated by e^{-1}. We stop after $\theta(r)$ and T_{phot} converge to $\lesssim 10\%$.

5.4.   The Choice of Assumptions

For modeling X-ray line emission from the disk atmosphere, the commonly used assumptions of LTE and the diffusion approximation will not hold. In addition, assuming a constant density in the vertical direction will be inadequate, since the hydrostatic equilibration time is small or comparable to other relevant timescales, and the line emission is highly sensitive to the vertical ionization structure. This is especially true for recombination emission, in which each ion has a characteristic set of line energies, and it contrasts with fluorescent line energies, which vary little with ionization state until the atom is almost fully ionized. Yet, even fluorescence emission can be affected by a Compton-thick, fully ionized gas above it (Nayakshin, Kazanas, & Kallman 2000).

Hydrostatic equilibrium, thermal equilibrium, and ionization equilibrium should be good assumptions in a time averaged sense. The radiation transfer is complex, and the assumptions used to simplify calculations could be problematic. In particular, by dividing the disk atmosphere into annular zones with a given vertical gas column, our 1-D radiation transfer calculation assumes that 1) the primary continuum is not absorbed before reaching the top of the column, 2) the radiation in the column propagates from top to bottom at a given grazing angle, and 3) there is no significant radiative coupling from one disk annulus to another, which is used to justify the slab approximation. The above assumptions are inadequate if the column height is comparable to the disk radius, or if the photon mean free path in the gas column is many times the local radius. Thus, future 2-D calculations will result in better bookkeeping of photons, a more accurate structure, and a more reliable X-ray line spectrum.

The correct calculation of line transfer in the gas is also a concern, since the disk atmosphere is optically thick in the lines. Line transfer is complicated by the Keplerian velocity shear, which has to be taken into account for a given viewing angle (Murray & Chiang 1997). The escape-probability approximation used to calculate line transfer in the disk may also be inadequate because of the large optical depths.

Our calculations show that the proper treatment of a thermal instability (Field 1965; Krolik, McKee, & Tarter 1981) and the effect of conduction to resolve it affect the spectrum significantly (Zeldovich & Pikelner 1969). A two-phase gas could form, with clouds of an unknown size distribution and with undetermined dynamics of evaporation and condensation (Begelman & McKee 1990), with each phase having distinct ionization parameter and opacity. The instability is sensitive to 1) the metal abundances, 2) the continuum shape (Hess, Kahn, & Paerels 1997), and 3) the atomic kinetics (Savin et al. 1999). Finally, the inclusion of radiation pressure in high luminosity systems or for small radii is advisable (Proga, Stone, & Kallman 2000).

The local viscous energy dissipation rate per unit volume in the disk atmosphere can be included in Eq. (21) with the form (SS73; Czerny & King 1989)

$$Q_{visc} = \frac{3}{2}\Omega\alpha P \qquad (26)$$

where Ω is the Keplerian angular velocity, α is the viscosity parameter, and P is the local total gas pressure. Equation (26) is an extension of the α-disk model, where the viscous dissipation is vertically averaged, assumes the local validity of the α prescription, and is untested. Fortunately, our numerical modeling indicates that the viscosity term is negligible in most regions of the disk atmosphere except for the inner disk if $\alpha \sim 1$ (in particular, near the Compton-temperature corona). Its effect is to enhance a thermal instability between 10^6 and 10^7 K. Vertically stratified MHD models (Miller & Stone 2000), although inconclusive, owing to the uncertain effect of boundary conditions, show that the viscous dissipation drops rapidly $\gtrsim 2$ pressure scale heights away from the disk midplane, providing evidence against Eq. (26). The disk atmosphere is always a few scale heights above the midplane. Therefore, we choose not to include this term in our models. Equation (26) has been applied in the optically thick regions of the disk (Dubus et al. 1999) and in the disk atmosphere (Rozanska & Czerny 1996). Other forms for the local dissipation that reduce to the α-disk have been used (Meyer & Meyer-Hofmeister 1982).

5.5. Thermal Instability

Irradiated gas is subject to a thermal instability for temperatures in the 10^5–10^6 K range (Buff & McCray 1974; Field, Goldsmith, & Habing 1969), suppressing X-ray line emission in that regime. The Field (1965) stability criterion indicates that a photoionized gas may become unstable when recombination cooling of H-like and He-like ions is important. The temperature and ionization parameter ranges where the instability occurs depend on the metal abundances and the local radiation spectrum (Hess, Kahn, & Paerels 1997). Within a range of *pressure ionization parameters* ($\Xi \equiv P_{rad}/P_{gas}$, where P_{rad} is the radiation pressure, and P_{gas} the gas pressure; Krolik, McKee, & Tarter 1981), thermal equilibrium is achieved by three distinct temperatures, only two of which are stable to perturbations in T (see Fig. 4). The instability implies a large temperature gradient as the gas is forced to move between stable branches, requiring the formation of a transition region whose size could be determined by electron heat conduction.

For simplicity, we neglect emission from the conduction transition region. Upon calculation of the Field length, the length scale below which conduction dominates thermal equilibrium, we estimate that conduction forms a transition layer $\sim 10^{-2}$ times the geometrical thickness of the X-ray emitting zones. Nevertheless, X-ray line emission from the neglected transition region could be important (Li, Gu, & Kahn 2001).

Consideration of conduction gives a physical interpretation to choosing one of the two stable solutions for a given Ξ. Roughly, a static conduction solution must split the instability region in half, taking the low-T stable branch at $\Xi < \Xi_{stat}$, and the high-T stable branch at $\Xi > \Xi_{stat}$, separated by the transition layer at Ξ_{stat} (Zeldovich & Pikelner 1969). A transition layer located away from Ξ_{stat} will dynamically approach Ξ_{stat} by mass flow. Thus, a transition layer at
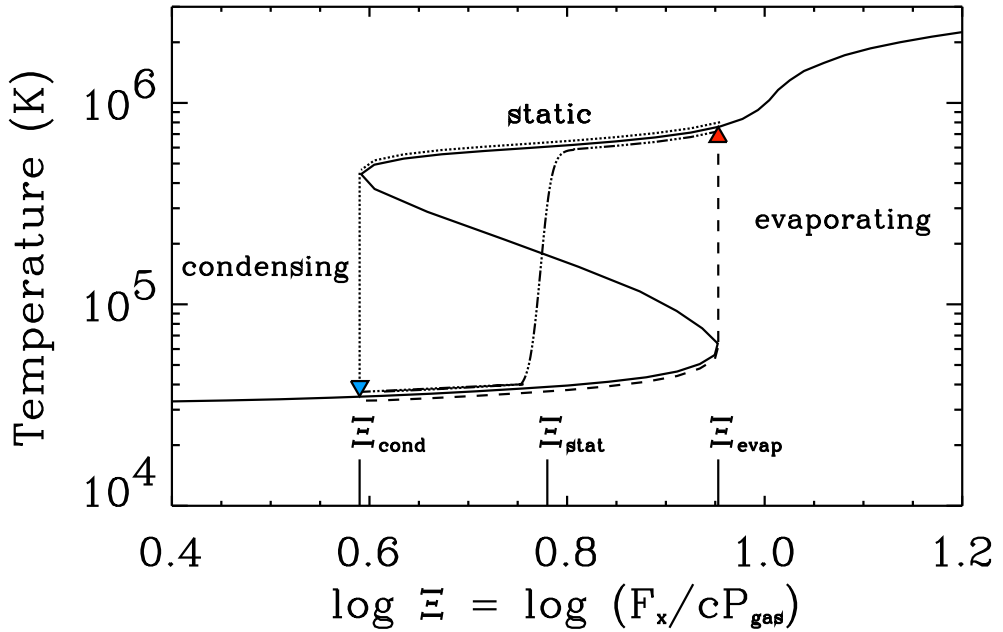
Figure 4.   Electron temperature vs. pressure ionization parameter, assuming an 8 keV bremsstrahlung for the spectral shape of the irradiating continuum. The solid S-curve corresponds to the locus of solutions of the equations of thermal balance and ionization equilibrium. Stable solutions have positive slope. We model the extreme cases, the evaporating and condensing disks, which correspond to the lower and upper stable branches of the curve, respectively. The inclusion of electron conduction modifies the S-curve to the dotted, dashed, or dash-dotted curves. The dash-dotted curve is a schematic of the static solution, the dotted curve corresponds to the extreme condensing solution, and the dashed curve to the extreme evaporating solution. Above $\Xi = 1.2$, the equilibrium temperature rises to the Compton temperature $\sim 10^7$ K (not shown).

$\Xi_{\text{evap}} > \Xi_{\text{stat}}$ corresponds to evaporating gas, while a transition at $\Xi_{\text{cond}} < \Xi_{\text{stat}}$ implies condensing gas (Zeldovich & Pikelner 1969).

We compute the disk structure for both condensing and evaporating solutions (Jimenez-Garate et al. 2001). The static conduction solution is an intermediate case of the latter extreme cases. We always take a single-valued $T(\Xi)$, since a two-phase solution may be buoyantly unstable, making the denser, colder gas sink. The evaporating disk corresponds to the low-T branch of the instability, while the condensing disk corresponds to the high-T branch.

5.6.   Preliminary Comparisons with Observed Spectra

Using a model for a disk illuminated by a neutron star, we have produced an X-ray recombination line spectrum from a self-consistent accretion disk atmosphere. The flaring of the atmosphere is consistent with optical observations (de Jong, van Paradijs, & Augusteijn 1996). By introducing the feedback between illumination and disk atmosphere geometry (see Eq. 25), we have obtained a disk with a height to radius (z_{atm}/r) ratio that is ~ 10 times larger than previously thought, with a corresponding increase in the reprocessed line radiation intensity.

With the disk structure $[\rho(r,z), \; T(r,z)]$ and charge state distributions $f_{Z,i}(r,z)$, we compute local X-ray emissivities using detailed atomic models. The atomic structure, radiative transition rates, and collisional rate coefficients are calculated with HULLAC (Hebrew University/Lawrence Livermore Atomic Code; Klapisch et al. 1977). Radiative recombination rates, including the RRC, are found from the Milne relation using the photoionization cross-sections provided by Saloman, Hubble, & Scofield (1988). The overall spectral model includes the H-like and He-like ions of C, N, O, Ne, Mg, Si, S, Ar, Ca, and Fe, as well as the Fe L-shell ions. Further details are described in Sako et al. (1999).

Each annulus consists of a grid of zones in the vertical direction, and T, ρ and $f_{Z,i+1}$ for each zone are used to calculate the line and RRC emissivities. The radiation is propagated outwards at inclination angle i, including the continuum opacity of all zones above. The spectrum is Doppler broadened by the projected local Keplerian velocity, assuming azimuthal symmetry. The outgoing spectrum for each annulus is added to a running total to obtain the total disk spectrum.

Our models show that, for a low-inclination LMXB, X-ray lines from the disk will be difficult to detect against the bright continuum. The *Chandra* LETGS spectrum of X0614+091 (Paerels et al. 2001) confirms this. Although a number of interstellar absorption features are present, there is no evidence for disk line emission. The data can be reproduced, i.e., we can generate a model spectrum for which the X-ray line emission lies below the limit of detectability, if we constrain the outer disk radius such that $r \lesssim 10^{10}$ cm. We propose that this source is at a low inclination and has a small accretion disk, reducing substantially the equivalent widths of disk emission lines. Unfortunately, the orbital parameters and inclination of this source are unknown. Of course, this is only a consistency check—not the best way to corroborate details of disk models—but it is still somewhat gratifying that there are plausible pockets of parameter space for which the model predicts unobservably weak lines.

The *XMM-Newton* RGS spectrum of X0748-67, which shows a number of emission lines (§5.1), provides a more stringent test. We have not yet attempted
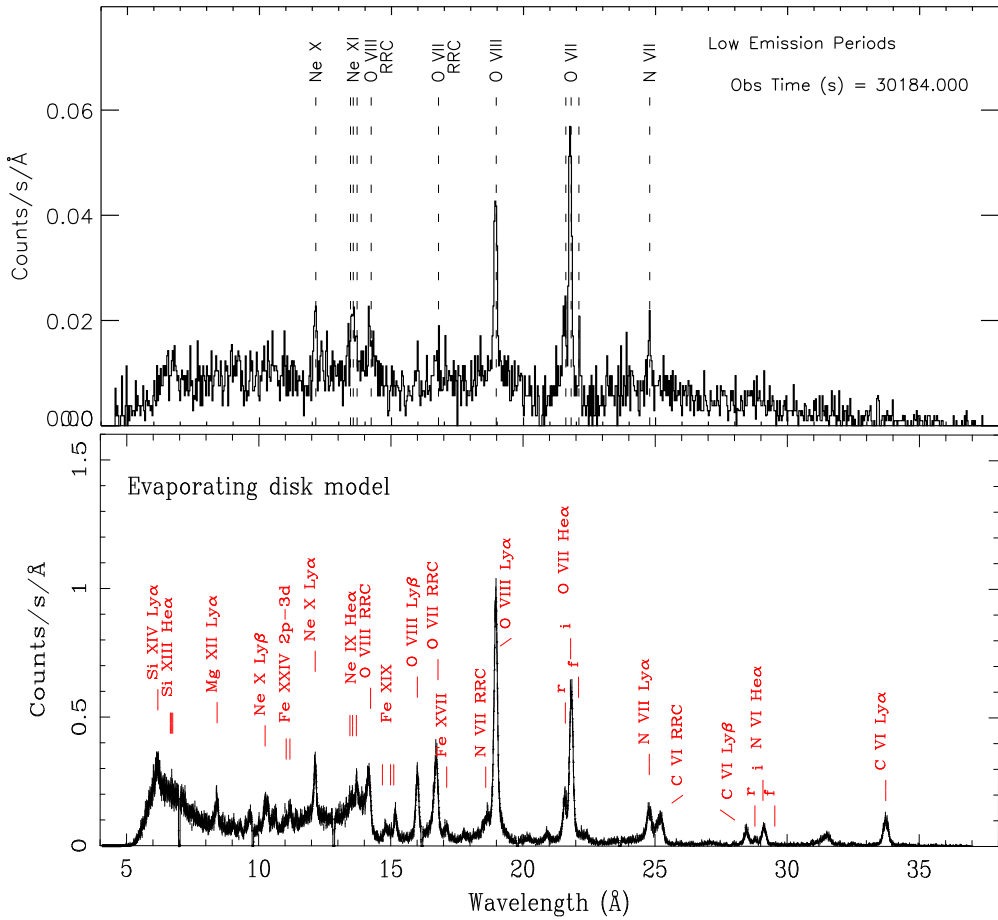
Figure 5.   *Top:* Spectrum of X0748-67 observed with the *XMM-Newton* RGS during 30 ks of low (dipping) states (from Cottam et al. 2000). *Bottom:* Simulated spectrum of a 50 ks observation for an Eddington luminosity LMXB at 10 kpc, with $N_H = 5 \times 10^{22}$ cm^{-2} for the central flux, and $N_H = 10^{21}$ cm^{-2} for the disk emission.

to "fit" the data; the particular result discussed here arises from a preliminary investigation of the sensitivity of the X-ray line spectrum to parameter variation and selecting among different thermally stable solutions (Jimenez-Garate et al., in preparation). As can be seen from (Fig. 5), our disk atmosphere model spectrum compares favorably with the X0748-67 data. The model disk inclination is set to 75°. For the line emission, we applied a neutral absorbing column density $N_H = 10^{21}$ cm^{-2}, and for the continuum emission $N_H = 5 \times 10^{22}$ cm^{-2}, which represents a geometry for which a compact continuum source is obscured by material in the outer disk. This is consistent with the significant variability in the continuum, and the absence of variability in the extended disk line emission. Integration of theoretical He-like spectra over the disk produce He-like R ratios that are consistent with those observed. For example, the typical model atmospheric density corresponding to O VII emission is $n_e \sim 10^{14}$ cm^{-3} or greater. Hydrogen-like O VIII RRC are very broad, with a superposed narrow component in evaporating disks. The O VII RRC and the w line appear at the expected relative levels. Among other preliminary results, we find that the O VIII/O VII line ratios are good tracers of evaporation from the disk (Jimenez-Garate et al. 2001), so that the predicted O VIII Lyα to O VII Heα ratio, for example, is sensitive to both the flaring angle of the disk and to the presence or absence of evaporation. The robustness of the calculated ratio against changes in the computational methods used will have to be evaluated *vis-a-vis* other models, e.g., those using 2-D radiation transfer. The O VII Heα line flux may be more model dependent since it is produced in a smaller region, where conduction is not negligible.

Line profiles for X0748-67are resolvable by the *XMM* and *Chandra* spectrometers. We find that an essential factor in properly calculating line profiles is that X-ray line formation, for a given line, is spread over most of the disk. For example, the dL/dr profile of O VIII Lyα (Fig. 6) shows that radii spanning several orders of magnitude ($10^{8.5} \leq r \leq 10^{11}$ cm) need to be accounted for (this applies also, of course, to a proper calculation of the total line luminosity or line equivalent width). The theoretical line profile for a single narrow annulus is double peaked. However, integrated over the disk surface, the line acquires broad, smooth wings and only a very narrow double- peaked core from the outermost annulus. The spectrometer response can easily smooth this feature into a quasi-Gaussian core profile. Again we see that access to a global, parameterized model of the source is imperative if we are to provide a valid interpretation—not just a description—of spectroscopic data. The erstwhile goal of inferring accretion disk structure by working backwards from a set of plasma diagnostics appears to be an untenable proposition.

6.   Final Comments

We have remarked that, thus far, X-ray emission line spectra of XRBs consist almost exclusively of H-like and He-like ion spectra, mixed with Kα fluorescence lines. While the atomic physics and population kinetics of the former are fairly simple, the latter are, in principle, quite complicated, but merely *treated* as though they were simple. To some extent, this situation removes the atomic physics barriers to successful interpretations of X-ray spectra from
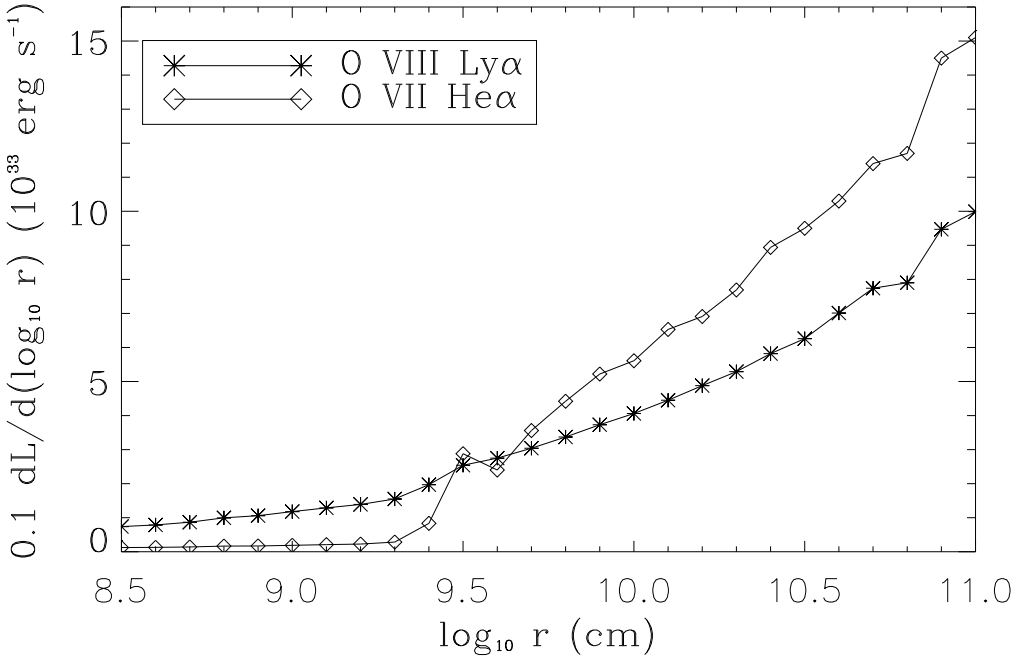
Figure 6.   Luminosity per bin as a function of radius of the lines from
H-like and He-like oxygen for the disk atmosphere model described in
§5.3. Each line is emitted throughout a large region of the disk.

XRBs. With increasing detector areas, however, such as will become available
with *Constellation-X*, more advanced techniques will become more readily avail-
able (Fe L-shell spectroscopy, ion fluorescence spectroscopy, etc.). At that time,
atomic physics issues and uncertainties will again be a primary concern. For the
time being, it is our opinion that there are more pressing problems.

As has been discussed, line formation in an XRB is inherently global, in
the sense that line luminosities typically involve integrations over non-negligible
fractions of the source volumes, over which the basic physical parameters may
assume a broad range of values. Although it is useful to derive semi-quantitative
estimates of densities, temperatures, and velocities from observed spectra, the
notion that a particular value of a particular diagnostic line ratio allows us to
specify one of these physical parameters fails to acknowledge this global nature.
What is needed, therefore, is development of and access to global models of
XRBs—models that strive for spectroscopic accuracy, so that X-ray spectra
now being obtained with *Chandra* and *XMM-Newton* can be used as feedback.
We have described a few of these models. Those that have been successful at
reproducing X-ray spectra are full of simplifying assumptions, thereby lacking
sufficient physical realism. Unfortunately, adding complexity to models does
not guarantee their success, owing to the need to select among various subsets
of physical assumptions. In the long term, radiative-hydrodynamic calculations
will undoubtedly provide an increasingly realistic picture of accretion flows in
XRBs. In the near term, however, we are faced with a number of obstacles, both
conceptual and practical, that remain to be surmounted.

References

Abramowicz, M.A., Czerny, B., Lasota, J.P., & Szuszkiewicz, E. 1988, ApJ, 332, 646

Asai, K., Dotani, T., Nagase, F., & Mitsuda, K. 2000, ApJS, 131, 571

Balbus, S.A. & Hawley, J.F. 1998, Rev. Mod. Phys., 70, 1

Bautista, M.A. & Kallman, T.R. 2000, ApJ, 544, 581

Becker, R.H., Pravdo, S.H., Rothschild, R.E., Boldt, E.A., Holt, S.S., Serlemitsos, P.J., & Swank, J.H. 1978, ApJ, 221, 912

Begelman, M.C. & McKee, C. 1990, ApJ, 358, 375

Blandford, R.D. & Begelman, M.C. 1999, MNRAS, 303, 1

Blondin, J.M. 1994, ApJ, 435, 756

Blondin, J.M., Kallman, T.R., Fryxell, B.A., & Taam, R.E. 1990, ApJ, 356, 591

Blondin, J.M. & Woo, J.W. 1995, ApJ, 445, 889

Blumenthal, G.R,. Drake, G.W.F., & Tucker, W.H. 1972, ApJ, 172, 205

Bondi, H. & Hoyle, F. 1944, MNRAS, 104, 273

Bolton, C. 1971, Bull. AAS, 3, No. 4

Brandt, W.N. & Schulz, N.S. 2000, ApJ, 544, L123

Buff, J. & McCray, R. 1974, ApJ, 189, 147

Carlberg, R.G. 1980, ApJ, 241, 1131

Castor, J.I., Abbott, D.C., & Klein, R.I. 1975, ApJ, 195, 157

Chen, X., Abramowicz, M.A., Lasota, J., Narayan, R., & Yi, I. 1995, ApJ, 443, L61

Chen, X. & Taam, R.E. 1993, ApJ, 412, 254

Church, M.J. 2000, preprint, astro-ph/0012411

Church, M.J. & Balucinska-Church, M. 1993, MNRAS, 260, 59

Church, M.J. & Balucinska-Church, M. 1995, A&A, 300, 441

Church, M.J., Balucinska-Church, M., Dotani, T., & Asai, K. 1998, ApJ, 504, 516

Church, M.J., Dotani, T., Balucinska-Church, M., Mitsuda, K., Takahashi, T., Inoue, H. & Yoshida, K. 1997, ApJ, 491, 388

Clark, G.W., Minato, J.R., & Mi, G. 1988, ApJ, 324, 974

Cottam, J., Kahn, S.M., Brinkman, A.C., den Herder, J.W. & Erd, C. 2001, A&A, 365, L277

Czerny, M. & King, A.R. 1989, MNRAS, 236, 843

Davidson, K. & Netzer, H. 1979, Rev. Mod. Phys., 51, 715

Davidsen, A. & Ostriker, J.P. 1974, ApJ, 189, 331

de Jong, J.A., van Paradijs, J., & Augusteijn, T. 1996, A&A, 314, 484

Dubus, G., Lasota, J.P., Hameury, J.M., & Charles, P. 1999, MNRAS, 303, 139

Dupree, A.K., et al. 1980, ApJ, 238, 969

Eardley, D.M., Lightman, A.P., & Shapiro, S.L. 1975, ApJ, 199, L153

Ebisawa, K., et al. 1996, PASJ, 48, 425

Ferland, G.J., Korista, K.T., Verner, D.A., Ferguson, J.W., Kingdon, J.B., & Verner, E.M. 1998, PASP, 110, 761

Field, G.B. 1965, ApJ, 142, 531

Field, G.B., Goldsmith, D.W., & Habing, H.J. 1969, ApJ, 155, L149

Frank, J., King, A., & Lasota, J.-P. 1987, A&A, 178, 137

Frank, J., King, A., & Raine, D. 1992, *Accretion Power in Astrophysics, Second Edition* (Cambridge University Press)

Fryxell, B.A. & Taam, R.E. 1988, ApJ, 335, 682

Gabriel, A.H. & Jordan, C. 1969, MNRAS, 145, 241

Garcia, M.R., McClintock, J.E., Narayan, R., Callanan, P., Murray, S.S. 2000, astro-ph/0012452

Glass, I.S. 1994, MNRAS, 268, 742

Haberl, F., White, N.E., & Kallman, T.R. 1989, ApJ, 343, 409

Hammerschlag-Hensberge, G., Kallman, T. R., & Howarth, I. D. 1984, ApJ, 283, 249

Hatchett, S. & McCray, R. 1977, ApJ, 211, 552

Hess, C.J., Kahn, S.M., & Paerels, F.B.S. 1997, ApJ, 478, 94

Hirano, T., Hayakawa, S., Nagase, F., Masai, K., & Mitsuda, K. 1987, PASJ, 39, 619

Ichimaru, S. 1977, ApJ, 214, 840

Jacobs, V.L., Doschek, G.A., Seely, J.F., & Cowan, R.D. 1989, Phys. Rev, A, 39, 2411

Jimenez-Garate, M.A., Raymond, J.C., Liedahl, D.A., & Hailey, C. 2001, ApJ, submitted

Johnston, H.M., Fender, R., & Wu, K. 1999, MNRAS, 308, 415

Kahn, S.M., et al. 2001, A&A, 365, L312

Kallman, T.R., Liedahl, D.A., Osterheld, A.L., Goldstein, W.H., & Kahn, S.M. 1996, ApJ, 465, 994

Kallman, T.R. & McCray, R. 1982, ApJS, 50, 263

Kallman, T.R. & Krolik, J.H. 1999, XSTAR v1.43, HEASARC (NASA/GSFC), Greenbelt, MD

Kaper, L., Henrichs, H.F., Nichols, J.S., Snoek, L.C., Volten, H., & Zwarthoed, G.A.A. 1996, A&AS, 116, 257

Kiplinger, A.L. 1979, ApJ, 234, 997

Klapisch, M., Schwab, J.L., Fraenkel, J.S., & Oreg, J. 1977, J. Opt. Soc. Am., 61, 148

Ko, Y. & Kallman, T.R. 1991, ApJ, 374, 721

Ko, Y. & Kallman, T.R. 1994, ApJ, 431, 273

Krolik, J.H., McKee, C.F., & Tarter, C.B. 1981, ApJ, 249, 422

Krzemiński, W. 1974, ApJ, 192, L135

Lamb, F.K. 1989, in *Proc. 23rd ESLAB Symp. on Two Topics in X-ray Astronomy*, ed., J. Hunt & B. Battrick (ESA SP-296) (Paris: ESA), p. 215

Lamb, F.K. & Miller, M.C. 1995, ApJ, 439, 828

Lewin, W.H.G., van Paradijs, J., & van den Heuvel, E.P.J., eds., *X-ray Binaries* (Cambridge University Press: Cambridge)

Lewis, W., Rappaport, S., Levine, A., & Nagase, F. 1992, ApJ, 389, 665

Li, Y., Gu, M.F., & Kahn, S.M. 2001, ApJ, submitted

Liedahl, D.A. 1999, in *X-Ray Spectroscopy in Astrophysics*, eds., J. van Paradijs and J. Bleeker, Springer Lecture Notes in Physics, p. 189

Liedahl, D.A., Kahn, S.M., Osterheld, A.L., and Goldstein, W.H. 1990, ApJ, 350, L37

Liedahl, D.A., Kahn, S.M., Osterheld, A.L., and Goldstein, W.H. 1992, ApJ, 391, 306

Liedahl, D.A. & Paerels, F. 1996, ApJ, 468, L33

Liedahl, D.A., Sako, M., Wojdowski, P.S., Paerels, F., and Kahn, S.M. 2000, RevMexAA (Serie de Conferencias), 9, 40

Lucy, L.B. 1982, ApJ, 255, 286

Lucy, L.B. & White, R.L. 1980, ApJ, 241, 300

Luo, C. & Liang, E.P. 1998, ApJ, 498, 307

MacGregor, K.B., Hartman, L., & Raymond, J.C. 1979, ApJ, 231, 514

MacGregor, K.B. & Vitello, P.A. 1982, ApJ, 259, 267

Malkan, M.A. 1983, ApJ, 268, 582

Masai, K. 1984, Ap&SS, 106, 391

Matt, G., Fabian, A.C., & Ross, R.R. 1993, MNRAS, 262, 179

McClintock, J.E., London, R.A., Bond, H.E. & Grauer, A.D. 1982, ApJ, 258, 245

Mewe, R. 1999, in *X-Ray Spectroscopy in Astrophysics*, eds., J. van Paradijs and J. Bleeker, Springer Lecture Notes in Physics, p. 109

Meyer, F. & Meyer-Hofmeister, E. 1982, A&A, 106, 34

Miller, K.A. & Stone, J.M. 2000, ApJ, 534, 398

Mitsuda, K., et al. 1984, PASJ, 36, 741

Morton, C.D. 1967, ApJ, 150, 535

Murray, N. & Chiang, J. 1997, ApJ, 474, 91

Nagase, F. 1989, PASJ, 41, 1

Nagase, F., Hayakawa, S., Makino, F., Sato, N., & Makishima, K. 1983, PASJ, 35, 47

Nagase, F., Zylstra, G., Sonobe, T., Kotani, T., Inoue, H., & Woo, J. 1994, ApJ, 436, L1

Narayan, R., & Yi, I. 1995, ApJ, 452, 710

Nayakshin, S., Kazanas, D., & Kallman, T.R. 2000, ApJ, 537, 833

Osterbrock, D.E. 1989, *Astrophysics of Gaseous Nebulae and Active Galactic Nuclei* (University Science Books)

Owocki, S.P. & Rybicki, G.B. 1984, ApJ, 284, 337

Paerels, F., et al. 2000, ApJ, 533, L135

Paerels, F., et al. 2001, ApJ, 546, 338

Parmar, A.N., White, N.E., Giommi, P., & Gottwald, M. 1986, ApJ, 308, 199

Pauldrach, A., Puls, J., & Kudritzki, R.P. 1986, A&A, 164, 86

Phillips, K.J.H., et al. 1982, ApJ, 256, 774

Porquet, D., & Dubau, J. 2000, A&A, 143, 495

Pradhan, A.K. 1982, ApJ, 263, 477

Pradhan, A.K. 1985, ApJ, 288, 824

Prendergast, K.H. & Burbidge, G.R. 1968, ApJ, 151, L83

Press, W.H. 1994, Numerical Recipes in FORTRAN : The Art of Scientific Computing (Cambridge: Cambridge University Press)

Pringle, J.E., Verbunt, F., & Wade, R.A. 1986, MNRAS, 221, 169

Proga, D., Stone, J.M. & Kallman, T.R. 2000, ApJ, 543, 686

Psaltis, D., Lamb, F.K., & Miller, G.S. 1995, ApJ, 454, L137

Quataert, E. & Gruzinov, A. 2000, ApJ, 539, 809

Raymond, J.C. 1993, ApJ, 412, 267

Ross, R.R. & Fabian, A.C. 1993, MNRAS, 261, 74

Rozanska, A. & Czerny, B. 1996, Acta Astronomica, 46, 233

Sako, M., Liedahl, D.A., Paerels, F., & Kahn, S.M. 1999, ApJ, 525, 921

Saloman, E.B., Hubble, J.H., & Scofield, J.H. 1988, At. Data Nucl. Data Tables, 38, 1

Sato, N., Hayakawa, S., Nagase, F., Masai, K., Dotani, T., Inoue, H., Makino, F., Makishima, K., & Ohashi, T. 1986, PASJ, 38, 731

Savin, D.W. et al. 1999, ApJS, 123, 687

Schreier, E., Levinson, R., Gursky, H., Kellogg, E., Tananbaum, H., & Giacconni, R. 1972, ApJ, 172, L79

Schulz, N.S. 1999, ApJ, 511, 304

Schulz, N.S., Canizares, C.R., Huenemoerder, D., & Lee, J.C. 2000, ApJ, 545, L135

Seward, F.D., Forman, W.R., Giacconi, R., Griffiths, R.E., Harnden, F.R., Jr., Jones, C., & Pye, J.P. 1979, ApJ, 234, L55

Shakura, N.I. & Sunyaev, R.A. 1973, A&A, 24, 337 (SS73)

Shirey, R.E., Bradt, H.V., & Levine, A.M. 1999, ApJ, 517, 472

Shklovsky, I.S. 1967, ApJ, 148, L1

Stevens, I.R. 1991, ApJ, 379, 310

Stevens, I.R. & Kallman, T.R. 1990, ApJ, 365, 321

Sunyaev, R.A. & Titarchuk, L.G. 1980, A&A, 86, 121

Taam, R.E. & Fryxell, B.A. 1989, ApJ, 339, 297

Tanaka, Y. & Lewin, W.H.G. 1995, in *X-ray Binaries*, ed., W.H.G. Lewin, J. van Paradijs, & E.P.J. van den Heuvel (Cambridge University Press: Cambridge), p. 126

Tanaka, Y. & Shibazaki, N. 1996, ARA&A, 34, 607

Tarter, C.B., Tucker, W.H., & Salpeter, E.E. 1969, ApJ, 156, 943

Tennant, A.F., Fabian, A.C., & Shafer, R.A. 1986, MNRAS, 221, 27P

Trümper, J., Pietsch, W., Reppin, C., Voges, W., Staubert, R., & Kendziorra, E. 1978, ApJ, 219, L105

Vacca, W.D., Sztajno, M., Lewin, W.H.G., Truemper, J., van Paradijs, J., & Smith, A. 1987, A&A, 172, 143

van Paradijs, J. 1995 in *X-Ray Binaries*, ed., W.H.G. Lewin, J. van Paradijs, & E.P.J. van den Heuvel (Cambridge University Press: Cambridge), p. 536

Vrtilek, S.D., Boroson, B., Cheng, F.H., McCray, R., & Nagase, F. 1997, ApJ, 490, 377

Vrtilek, S.D., McClintock, J.E., Seward, F.D., Kahn, S.M., & Wargelin, B.J. 1991, ApJS, 76, 1127

Vrtilek, S.D., Raymond, J.C., Garcia, M.R., Verbunt, F., Hasinger, G., & Kurster, M. 1990, A&A, 235, 162

Wade, R.A. 1984, MNRAS, 208, 381

Waldron, W.L. & Cassinelli, J.P. 2000, astro-ph/0012190

Webster, B.L. & Murdin, L. 1972, Nature, 235, 37

Wheaton, W.A., et al. 1979, Nature, 282, 240

White, N.E. 1989, A&A Rev., 1, 85

White, N.E. & Holt, S.S. 1982, ApJ, 257, 318

White, N.E. & Mason, K.O. 1985, Space. Sci. Rev., 40, 167

White, N.E., Nagase, F., & Parmar, A.N. 1995, in *X-ray Binaries*, ed., W. H. G. Lewin, J. van Paradijs, & E. P. J. van den Heuvel (Cambridge University Press: Cambridge), p. 1

White, N.E., Parmar, A.N., Sztajno, M., Zimmermann, H.U., Mason, K.O., & Kahn, S.M. 1984, ApJ, 283, L9

White, N.E., Peacock, A., & Taylor, B.G. 1985, ApJ, 296, 475

White, N.E., Stella, L., & Parmar, A.N. 1988, ApJ, 324, 363

White, N.E., Swank, J.H., & Holt, S.S. 1983, ApJ, 270, 711

White, N.E., et al. 1994, PASJ, 46, L97

Wojdowski, P.S., Clark, G.W., & Kallman, T.R. 2000, ApJ, 541, 963

Wojdowski, P.S., Liedahl, D.A., & Sako, M. 2001, ApJ, 547, 973

Woo, J.W., Clark, G.W., Blondin, J.M., Kallman, T.R., & Nagase, F. 1995, ApJ, 445, 896

Zeldovich, Y.B. & Pikelner, S.B. 1969, Soviet Physics JETP, 29, 170

Zycki, P.T., Krolik, J.H., Zdziarski, A.A., & Kallman, T.R. 1994, ApJ, 437, 597